CHAPTER 1

MULTIFERROIC MATERIALS

1.1 Single Phase Multiferroic Materials

Multiferroic materials, also known as magnetoelectric or ferroelectromagnetic materials, exhibit both a magnetization and dielectric polarization in a single phase. This can result in the magnetoelectric effect[1] due to the coupling of the magnetic and dielectric ordering. The magnetoelectric effect is an induction of magnetization by an electric field or the induction of a dielectric polarization by a magnetic field. This effect has many proposed applications[2]. These might include devices for wave modulators, novel memory devices, switches, optical diodes, spin-wave generators, amplifiers among others.

The magnetoelectric effect was first confirmed experimentally in the antiferromagnetic system of Cr_2O_3 in 1960[3]. A relatively small number of other single phase multiferroics were later identified[1] although most have a very small magnetoelectric effect that is likely too weak for any practical application. The majority of these also have a critical temperature for the magnetic or dielectric properties that is much below room temperature. The low number and weak magnetoelectric effect is likely due to the mechanisms of ferroelectricity and magnetism being very different and often contradictory. For example, it has been proposed that ferroelectricity in many perovskite materials is due to a shift of the A and B cations relative to the oxygen octahedron due to ligand field stabilization in which the formally filled 2p states donate density into formally empty d states of the transition metal B cation[4]. Magnetism requires unpaired electrons which most often results from partially filled d shells. Hill and Filippetti[5, 6] proposed a d^0 rule which states that multiferroic properties are inhibited in perovskite materials because

ferroelectric displacement requires a d^0 state while magnetism requires a partially filled d orbital.

The d^0 rule helps to understand the possible contradictions between mechanisms needed to achieve single phase multiferroic materials; however it is far from conclusive. Many well known multiferroic materials ($BiMnO_3$, $LaMnO_3$, and BiFeO3 for example) have the perovskite structure. This requires a different mechanism for ferroelectricity than the suggested model. Theoretical research has shown that multiferroic materials are not inherently impossible with known mechanisms. It has been shown that there should be 18 space groups in total for which symmetry allows for both magnetism and ferroelectric properties[7]. The field of single phase multiferroics is relatively young and recently there has been a large increase in the amount of research in developing the understanding of single phase multiferroics.

1.2 Multiferroic Composites

Another promising method of achieving a technologically interesting multiferroic material involves the use of composites[8-11]. The first multiferroic composite was created from ferroelectric $BaTiO_3$ and ferromagnetic $CoFe_2O_4$ by unidirectional solidification in a eutectic composite[12]. Composites such as this have been shown to have much stronger magnetoelectric effects than for single phase materials[1]. This is due to the ability to combine materials with high permeability with materials with a high permittivity to achieve a high interaction. The magnetoelectric effect in a composite material is thought to mainly occur from mechanical coupling through piezoelectric and magnetostriction effects. This has resulted in much of the multiferroic work focusing on the interfaces between constituents. Focus on using laminar composites[13], has led to very good interfaces and therefore very good magnetoelectric response in composite multiferroics.

Nanocomposites are another large area of research in multiferroic materials. In this field, stacks of thin films of magnetic and dielectric materials are fabricated in a heterostructure. It is important to grow these films epitaxially to obtain single crystal films and strong interfacial interaction. Magnetic and dielectric properties of thin films have been shown to degrade as crystal quality decreases[14, 15]. Other nanostructure multiferroic materials also utilize single crystal films. Zheng et al[16] have made epitaixal nanopillars of $CoFe_2O_4$ surrounded by a $BaTiO_3$ matrix. They claim that this structure will eliminate substrate clamping that can lessen the piezoelectric-magnetostriction interaction. This material could possibly result in a higher magnetoelectric effect in a nanocomposite.

1.3 Conclusion

The coupling of magnetic properties with ferroelectric properties can have the possibility of many interesting applications. Unfortunately, the number of single phase multiferroics is limited due to the different and often contradictory mechanisms of magnetism and ferroelectric properties. A more promising method of obtaining a multiferroic material is through the use of composite materials. Laminated ceramics have shown magnetoelectric effects much higher than known single phase multiferroics. It has also been possible to scale these composites down to nanocomposites with limited success in the form of thin film heterostructures. Multiferroic materials are an interesting material for future applications.

CHAPTER 2

NEGATIVE INDEX OF REFRACTION

2.1 Introduction

The index of refraction is defined as the ratio of the speed of an electromagnetic wave in free space to the speed of the electromagnetic wave in a material with index of refraction n. The index of refraction can be shown to be related to the permeability and permittivity of a material by equation 2.1.

$$n \equiv \frac{c}{v} = \frac{1}{\pm\sqrt{\mu_r \varepsilon_r}} \tag{2.1}$$

This shows that there is an apparent velocity change in a material. This apparent velocity change can be visualized by examining Figure 2.1.

Figure 2.1 shows the effect of an electromagnetic wave when going from free space into a medium such as glass. The dotted lines show the position of the wave crests perpendicular to the propagation direction. It is expected that the wave oscillations at the surface of the glass must have the same frequency as in the vacuum. Given that the wavelength is given by $\lambda = 2\pi v/\omega$, the geometry requires that:

$$\frac{\lambda_0}{\sin\theta_0} = \frac{\lambda}{\sin\theta} \tag{2.2}$$

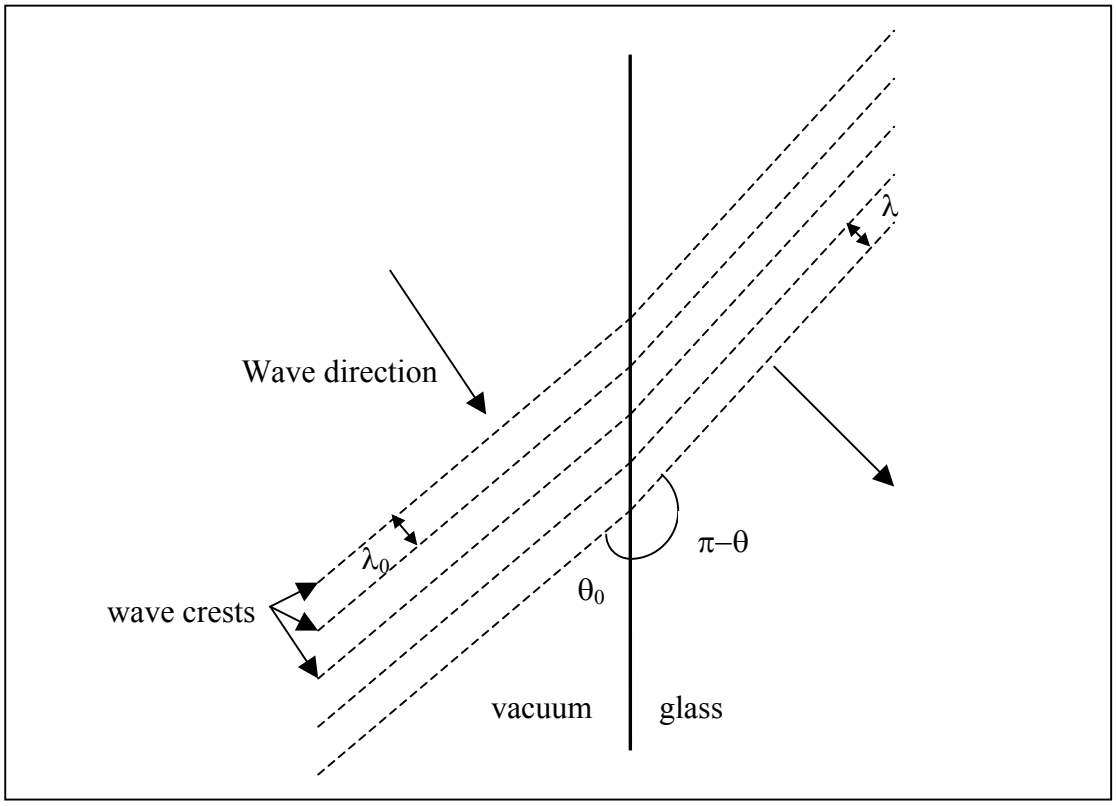

Figure 2.1: Effect of an electromagnetic wave as it enters glass from vacuum. The apparent velocity change is due to an apparent change of direction of the radiation.

We also know that the index of refraction is related to the wavelength change.

$$n = \frac{c}{v} = \frac{\lambda_0}{\lambda} \tag{2.3}$$

Comparison of Equation 2.2 with Equation 2.3 leads to Snell's Law for the case of light entering a material from free space.

$$n = \frac{\sin\theta_0}{\sin\theta} \tag{2.4}$$

2.2 The Dispersion Relationship

It is well known that the index of refraction is highly dependent on the frequency of the incident wave. The dispersion relationship for the index of refraction can be written as:

$$n = 1 + \frac{Nq_e^2}{2\varepsilon_0 m\left(\omega_0^2 - \omega^2\right)} \tag{2.5}$$

where N is the number of charges per unit volume in the material, q_e is the charge of an electron, ε_0 is the permittivity of free space, m is the mass of an electron, ω is the frequency of the wave, and ω_0 is the (dielectric) resonance frequency[17]. For light in most gases, the resonance frequency is high enough that the index looks constant versus frequency. For other materials, this is not the case. It can also be seen that interesting effects occur when the frequency is higher than the resonance frequency. When this occurs, the index of refraction is less than one. This means that the apparent velocity inside the material is greater than the speed of light in a vacuum. It must be stated that this does not mean that the *signal* moves faster in the material. The apparent velocity change is due to a phase shift explained by Figure 2.2[17].

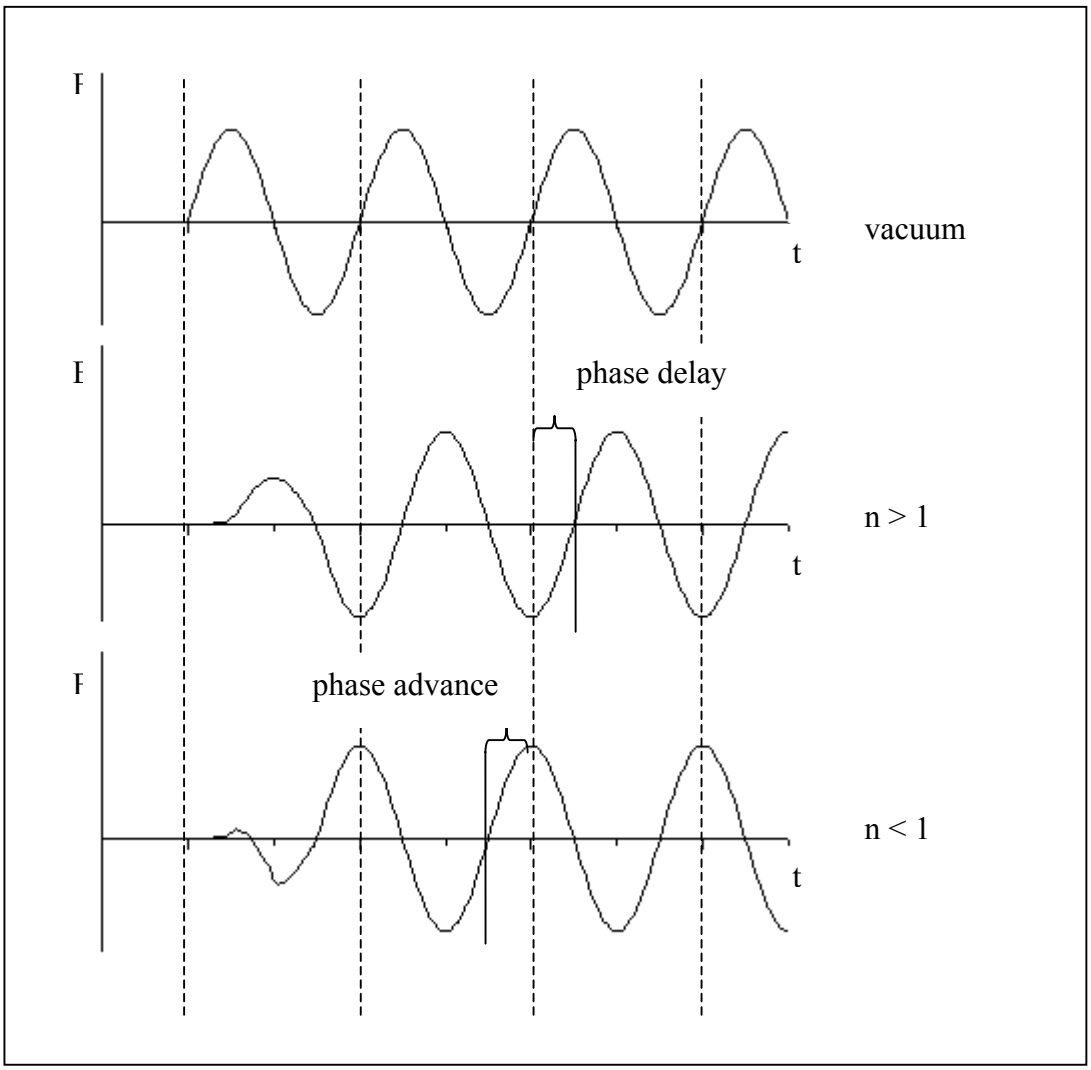

Figure 2.2: An electromagnetic signal entering a material of n>1 results in a phase delay, while a material of n<1 results in a phase advance. The phase advance does not result in an advance in the signal however.

When the index of refraction is greater than unity, there is a phase delay as expected. In the case where the index of refraction is less than unity, there is an apparent phase advance, although the signal has not been propagated faster. This apparent phase advance and interesting signal processing could be useful in some applications.

It should also be noted that the dispersion relationship is in reality much more complicated that Equation 2.5. First, the index of refraction has effects from both permittivity and permeability. Second, there are many resonance frequency modes for any material and the index of refraction has an effect from each. Third, each frequency mode with frequency ω_k also has a damping term $i\gamma_k\omega$. The effect from each frequency mode can then be summed to arrive at a new equation for dispersion:

$$n = 1 + \frac{q_e^2}{2\varepsilon_0 m}\sum_k \frac{N_k}{\omega_k^w - \omega^2 + i\gamma_k\omega} \tag{2.6}$$

The damping term makes the index of refraction a complex number. The imaginary part of the index of refraction is often termed the absorption index and is associated with the absorption of energy by the material. It can be seen that for frequencies near a resonance frequency the imaginary part becomes significant, limiting the usefulness of a possible index of refraction less than unity.

2.3 Negative Index of Refraction

The relationship of the index of refraction with the permittivity and the permeability of a material has been given in Equation 2.1. In 1968, Vesalago[18] postulated that if both the permeability and permittivity of a material are negative, then the negative value of the square root is taken. This results in a method of engineering a material with an index of refraction less than zero. This adds interesting effects such as negative group velocity and left-handed diffraction. Left-handed diffraction means that light bends in the opposite direction from that seen in Figure

2.1. A negative index material or left-handed material could be useful for many novel devices such as improved coupling in antennae[19], monolithic microwave integrated circuits[20], improved optics and lenses[21, 22] and other novel devices.

To date, there are no known homogeneous materials that exhibit both a negative permeability and negative permittivity at the same frequency[23]. These properties are generally associated with resonant behavior. It is unlikely that a single phase material will result in a magnetic and dielectric resonance at the same frequency, although it could be possible in a multiferroic if the magnetoelectric effect was large enough. A negative index material was realized experimentally in 2001 by Shelby, Smith and Schultz[24] using split ring resonators and wires to achieve the magnetic and dielectric resonance respectively. This resulted in a negative index of refraction in a small range of frequency in the GHz region. An effective negative index of refraction has also been realized through the use of photonic crystals[25]. Both of these methods rely on structure that is very near diffractive conditions. It is desirable to obtain a negative index of refraction using only intrinsic material properties that do not rely on structure near diffractive conditions. It should be possible to achieve this by creating a multiferroic composite that combines a dielectric resonance at a given frequency with a material that has a magnetic resonance at the same frequency.

2.4 Multiferroic Composite with a Negative Index of Refraction

Theoretical work has shown that a layered material with alternating layers of negative permittivity (and small permeability) and negative permeability (and small permittivity) will act as a material with an essentially negative index of refraction[26.27]. It should be possible to achieve this by creating a thin film heterostructure with alternating layers of negative permittivity and negative permeability using only intrinsic material resonances. There are three possible regions of electromagnetic

spectrum where it is thought viable to match a dielectric resonance and a magnetic resonance that would exhibit a negative excursion in the permittivity or permeability: the visible to ultraviolet region, the UHF to microwave region and the infrared region.

For the visible to ultraviolet region, there are many material choices for dielectric resonance. Electronic polarization modes tend to be in this region. These tend to be very lightly damped and often result in a frequency range of negative permittivity. The options for magnetic materials are less certain. It might be possible to find a ferromagnetic resonance in this region using a material with a very high anisotropy, but for known materials such as Co compounds, the maximum frequency is only expected to be about 100 GHz.

In the microwave frequency, there are many magnetic choices. Ferromagnetic resonances tend to be in the microwave region and are often very lightly damped. Ferromagnetic materials are well understood and often result in a negative permeability. Figure 2.3 shows the relative permeability of a yttrium iron garnet sample as a function of frequency as measured in the van Dover lab. A region of large negative permeability can be seen at a frequency higher than the resonance frequency. Dielectric polarization modes in the microwave region typically result in dipolar modes. These tend to be very highly damped and do not typically result in a negative excursion of the permittivity.

The infrared region appears to be more promising. Ionic modes in dielectric materials tend to be in this region. For example, $SrTiO_3$ has a frequency mode at about 100 cm^{-1} that softens as the temperature decreases toward the ferroelectric Curie temperature as seen in Figure 2.4[28]. Antiferromagnetic materials tend to have a magnetic resonance around 1THz. Table 2.1 summarizes the antiferromagnetic resonance frequency for several common antiferromagnetic materials[29]. It can be seen that there is a range of frequencies that result. It should be possible to engineer a

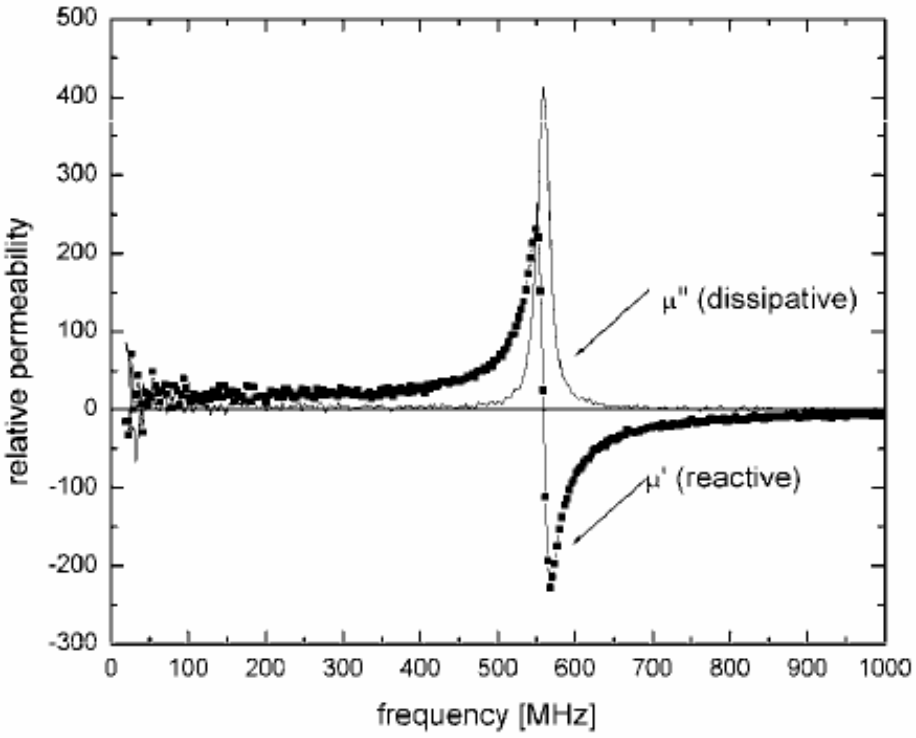

Figure 2.3: The frequency of dependence the relative permeability of a yttrium iron garnet sample. The resonance peak is due to a ferromagnetic resonance that results in a negative excursion in the permeability.

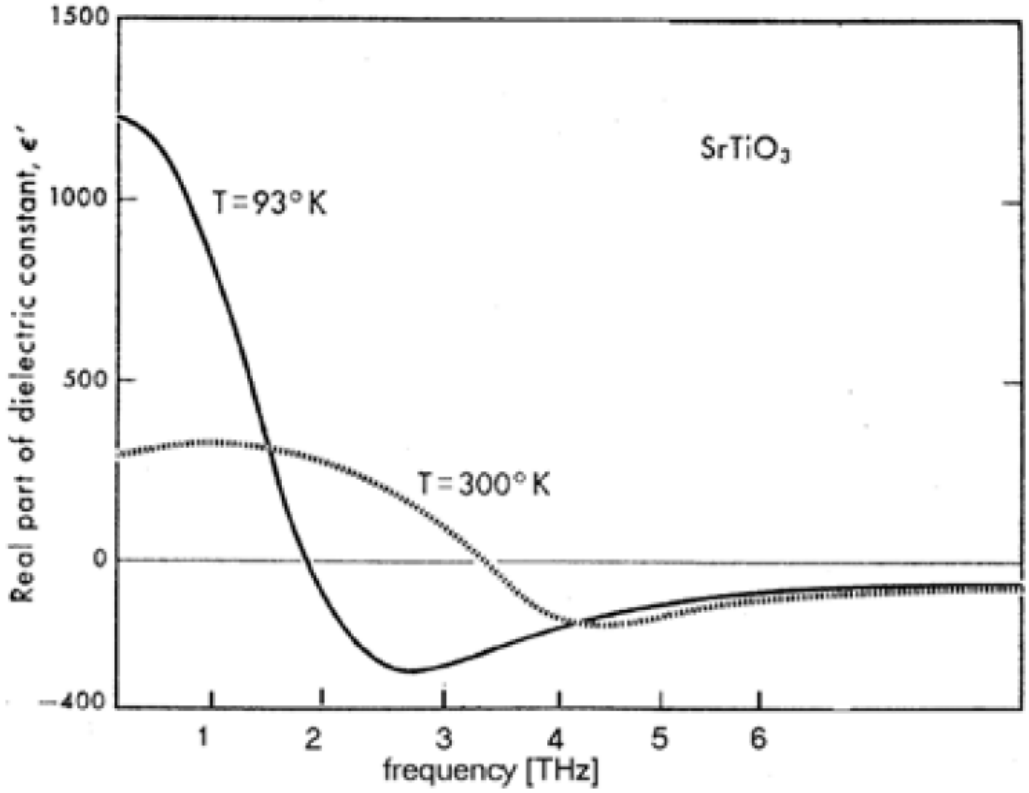

Figure 2.4: Real part of the dielectric constant of $SrTiO_3$ in the THz region. The phonon mode softens as the temperature decreases towards the ferroelectric Curie temperature ($T_c \approx 0K$).

material that matches an ionic resonance with an antiferromagnetic resonance in the far infrared region to achieve a negative index of refraction.

Table 2.1: Several antiferromagnetic materials with antiferromagnetic resonance frequency and Neel temperature.

Material	CoF_2	NiF_2	MnF_2	FeF_2	MnO	NiO	CoO[30]
Freq (THz)	0.855	0.933	0.260	1.58	0.828	1.09	~7
T_C (K)	Low	Low	Low	Low	~120	~520	~290

There are other possibilities of frequency responses that could be used to achieve a negative permeability or permittivity. Domain wall resonance in ferroelectrics could also be in the visible to ultraviolet range, however, these will likely be highly damped. Polymer materials might also exhibit dielectric resonances at some frequency that could be highly tunable. It might also be possible to couple strain in a multiferroic such that a strong ferromagnetic resonance could be coupled to a piezoelectric material. This could create a dielectric resonance that automatically matches the magnetic resonance. In order for this to work, the magnetostriction and piezoelectric response must have the correct orientation in order to obtain the magnetization 180° out of phase of H and polarization 180° out of phase of E. H and E are cross fields in electromagnetic radiation and therefore, the direction of strain in the material must account for this.

2.5 Negative Index of Refraction in the Far Infrared

It is proposed that if a material with an ionic resonance and a material with an antiferromagnetic resonance are combined in a composite material, it should be possible to engineer the resonances to match resulting in a negative index of refraction. It should be possible to fabricate this material in thin film form or as a bulk

ceramic. Thin film heterostructures could be useful for determining the effects of dopants on resonance frequency through the use of combinatorial approaches such as with off-axis sputtering[31]. This creates a need for materials with similar lattice constants in order to grow the heterostructure epitaxially due to the degradation of magnetic and ferroelectric properties as crystal quality decreases[14, 15]. It is proposed that antiferromagnetic NiO and perovskite $SrTiO_3$ should be epitaxially compatible and have resonances that can be tuned to match. They have a lattice mismatch of less than 7% and have resonances that should be possible to shift.

2.5.1 Tuning the NiO Antiferromagnetic Resonance

It is well known that the square of the antiferromagnetic resonance (AFMR) is proportional to the exchange field H_E and the effective anisotropy H_A as in Equation 2.7.

$$\omega_{AFMR}^2 \propto H_E H_A \tag{2.7}$$

This results in an AFMR frequency for NiO of about 36 cm^{-1}. It is known that Co^{2+} and Fe^{2+} have higher anisotropy energies than for Ni^{2+}. It is expected that doping NiO with Co^{2+} or Fe^{2+} will raise the AFMR frequency. Becker et al[32] have shown that this is indeed the case. They also show that the square of the AFMR frequency increases linearly with dopant concentration and that the slope is steeper for Co^{2+} doping for Fe^{2+} as expected. At a Co^{2+} doping level of about 6.6%, the AFMR frequency shifted to about 65 cm^{-1}. Fitting a line to this data results in an equation for the AFMR frequency of NiO as a function of Co^{2+} doping.

$$\omega_{AFMR}^2(NiO) \approx 443.8 X_{Co} + 1296 \qquad (cm^{-2}) \tag{2.8}$$

Becker et al were not able to measure the frequency response at a doping level higher than this due to the broadening of the resonance peak. It is unclear how high the resonance can be shifted before the peak becomes too broad to result in a negative excursion in the permeability.

2.5.2 Tuning the $SrTiO_3$ Dielectric Resonance

Cochran[32] proposed that a ferroelectric transition in certain crystals is associated with an optic mode of the lattice becoming unstable below the critical temperature. This frequency mode is finite above the Curie temperature and approaches zero as the temperature approaches the Curie temperature, becoming unstable at this temperature. A first approximation of the temperature dependence of this mode showed that the square of the mode frequency to be proportional to the difference between the temperature and the Curie temperature.

$$\omega^2 \propto (T - T_c) \tag{2.9}$$

Barker[33] used experimental data[28, 34] to fit an equation for the resonance frequency as a function of temperature for $SrTiO_3$.

$$\omega^2(SrTiO_3) \approx 35T - 1200 \qquad (\text{cm}^{-2}) \tag{2.10}$$

Equation 2.10 fits experimental data very well in the temperature range of 85K to 300K. Extrapolation to zero frequency suggests a Curie temperature of 34K for $SrTiO_3$. This is now known to be incorrect. This is likely due to higher order terms becoming more significant as the temperature approaches the Curie temperature, however, Equation 2.10 represents experimental data very well as long as the temperature is not close to the Curie temperature. Combining Equation 2.9 with Equation 2.10 leads to:

$$\omega^2(T, T_c) \approx 35(T - T_c) \qquad (\text{cm}^{-2}) \tag{2.11}$$

At room temperature:

$$\omega^2_{SrTiO_3} \approx -35T_c + 10500 \qquad (\text{cm}^{-2}) \tag{2.12}$$

Equation 2.12 should give an estimate of the response of the resonance to the change of Curie temperature due to doping as long as the Curie temperature does not approach room temperature. As T_c approaches room temperature, the linear approximation is no longer valid.

The Curie temperature of $SrTiO_3$ can be raised by doping with Ba. $(Ba,Sr)TiO_3$ is a well studied material for its high permittivity that results when the Curie temperature is increased to near room temperature. The Curie temperature of this material is about 300K for approximately 33% Ba. At doping levels less than 33%, it should be possible to systematically shift the Curie temperature from ~0K to 300K. This should result in a large range of possible resonance frequencies that shift as in Equation 2.12.

2.5.3 Matching NiO AFMR with $SrTiO_3$ dielectric resonance

It should be possible to engineer the resonances of NiO and $SrTiO_3$ to match at some frequency. The NiO AFMR has been shown to shift when doped with Co or Fe. It should also shift to higher frequency in the presence of an applied magnetic field. The $SrTiO_3$ should decrease with lowered temperature or with Ba doping. This leads to methods to several methods to verify the theory of a negative index in the far infrared. First, one could place a $NiO/SrTiO_3$ composite in an applied magnetic field which should shift the NiO AFMR to match the $SrTiO_3$ resonance if the field is large enough. Second, the composite could be cooled to low temperature which should decrease the resonance frequency of the $SrTiO_3$ to match the resonance of the NiO. Third, the NiO could be doped with Fe or Co and the $SrTiO_3$ could be doped with Ba to shift the resonance frequencies closer. The combination of the independent variables should allow for the matching of the NiO AFMR and the $SrTiO_3$ dielectric resonance.

The measurement of the high frequency response can be done with FTIR which has a radiation source that includes the frequency of interest. It should be straightforward to measure the frequency response of bulk materials, however, standard FTIR of thin films results in very poor signal to noise ratio. This can be

overcome through the use of polarized radiation or high intensity radiation from a synchrotron source[35, 36].

2.6 Conclusion

A material with a negative index of refraction has interesting and applicable properties. It is proposed that a composite material that combines an ionic dielectric resonance with an AFMR at the same frequency will have a negative index of refraction at that frequency. NiO has an AFMR at 36 cm^{-1} which should increase with an applied magnetic field or with Co or Fe doping. $SrTiO_3$ has a dielectric resonance at about 100 cm^{-1} that should decrease with decreasing temperature or with Ba doping. It should be possible to match these two resonances in a thin film heterostructure or a bulk ceramic composite to result in a material with a negative index of refraction in the far infrared.

CHAPTER 3

$NiO/SrTiO_3$ BULK CERAMIC COMPOSITE

3.1 Introduction

It has been proposed that a composite of NiO and $SrTiO_3$ might result in a material with a negative index of refraction. In order to fabricate a usable composite, these materials must be compatible and non-reacting under standard fabrication techniques. One method to study these materials is to use standard bulk ceramic techniques by pressing powders and sintering. X-ray diffraction can be used to identify phases and examine any lattice changes. FTIR spectroscopy can then be used to measure the high frequency response of the materials.

3.2 Technique

Bulk ceramics of NiO, $SrTiO_3$ and a 50/50 mole fraction composite of $NiO/SrTiO_3$ were fabricated from NiO and $SrTiO_3$ powders by standard processing techniques. For the composite sample, the powders were mixed in a mortar and pestle. Samples were pressed into 0.5 inch (1.27cm) diameter pellets of approximately 1 to 2 mm thick. Samples were pressed at a pressure of 100 MPa using isopropyl alcohol as a lubricant. The samples were sintered in air at temperatures ranging from 900 to 1550°C. The density of each sample was determined by measuring the mass on a balance and the volume with a micrometer. The theoretical density of $SrTiO_3$ is 5.175g/cm^3 and was achieved at 1400°C. The theoretical density of NiO is 6.67 g/cm^3. Only 80% of the expected density was achieved for NiO. There was no improvement in NiO density for temperatures above 1450°C. The density of the composite was found to be about 85% of the theoretical density for the composite. It should be possible to improve the density of the NiO and composite by hot pressing, although this has not been completed to data.

3.3 X-ray Diffraction Results

X-ray diffraction was used to identify any phases in the post sintered materials. Figure 3.1 shows the intensity versus 2θ plot for the composite material after sintering at 1550°C for 5 hours along with pure $SrTiO_3$ and pure NiO. It can be seen that the composite has only two phases, $SrTiO_3$ perovskite and NiO rocksalt structure. Neither phase shows evidence of shifted d spacing. This supports that NiO and $SrTiO_3$ are compatible and non-reacting even at high processing temperatures.

3.4 FTIR Measurements

FTIR is useful for finding the frequency response of the optical properties of a material in the infrared region. Standard FTIR does not typically cover the frequency range that is needed for this work. A special source that can extend below 100 cm^{-1} is needed. The measurements presented here have been completed by Mark Lee at Sandia National Labs in Albuquerque, NM.

Prior to measurement, the samples were polished by 1000 grit paper to assure a smooth surface for measurements. Care had to be taken due to the low density of the samples containing NiO. Figure 3.2 shows the FTIR results in reflectivity for a $SrTiO_3$ sample. The kink located at about 175 cm^{-1} is thought to be due to a twisting of a Ti-O bond of the lattice[36, 37]. This frequency mode is not expected to be useful for this project. The broad peak at about 100 cm^{-1} is the peak of interest. This peak is expected to soften with Ba doping and has been shown to exhibit a negative excursion in the permittivity[28]. It was found to be difficult to determine accurate permittivity values from this data using Kramer-Kronig analysis due to the high level of noise at low frequency. Kramer-Kronig requires integration from zero to infinity. The additional small peaks at other frequency are from excess water in the measurement system.

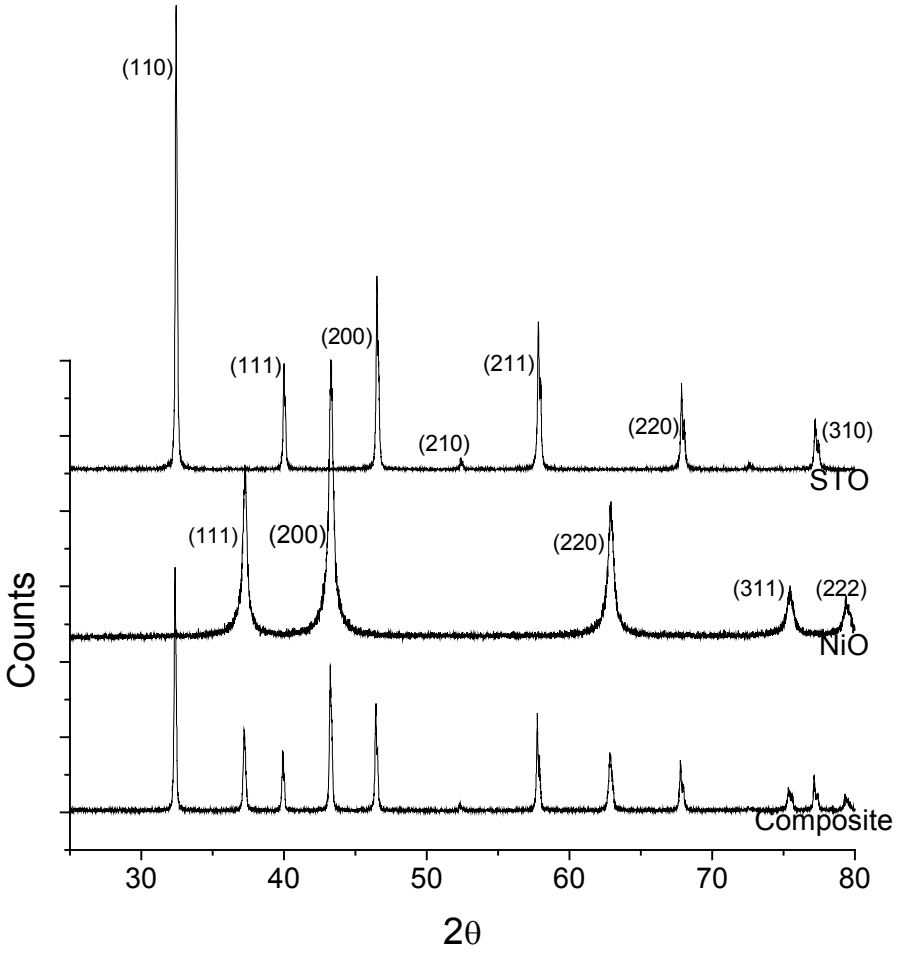

Figure 3.1: XRD data for NiO/$SrTiO_3$ composite compared to pure NiO and pure $SrTiO_3$. There is no evidence of reaction or shift in d spacing.

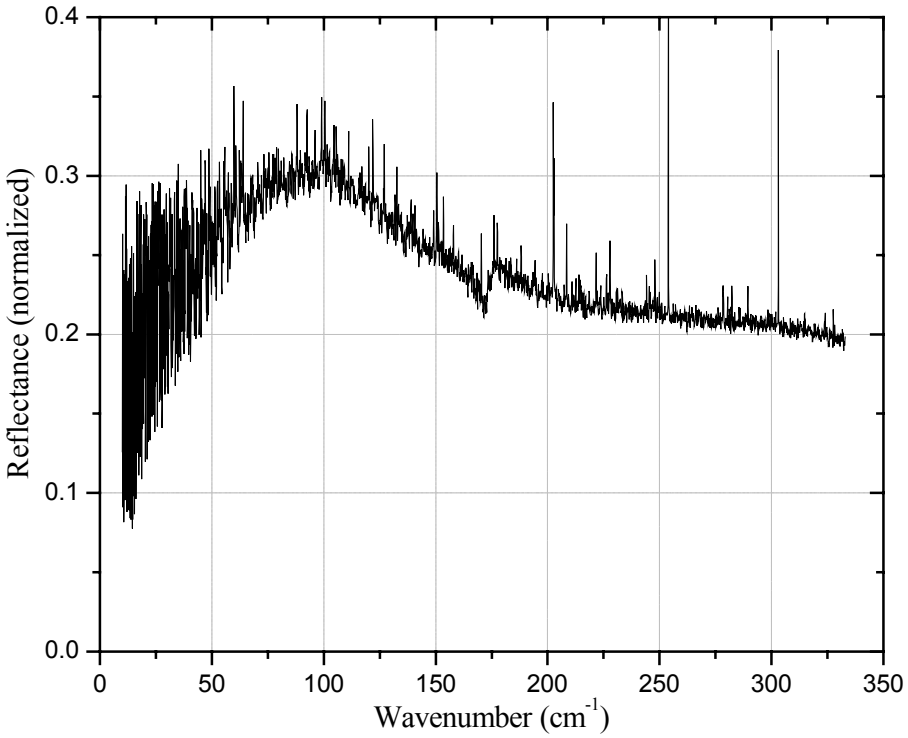

Figure 3.2: FTIR Reflectance results for a pressed powder $SrTiO_3$ sample. The ionic resonance is seen as the large broad peak around 100 cm^{-1}. There is also a kink around 175cm^{-1}. It is unclear how this peak might be shifted.

Figure 3.3 shows the frequency response of the NiO AFMR. First, it can be seen that the reflectivity for this sample is much lower than for the $SrTiO_3$ sample. This could be due to intrinsic material properties, but could also be due to the low density of the NiO sample. The AFMR peak is easily seen at the expected frequency of about 35 cm^{-1}. Figure 3.4 shows the frequency response for the composite material. The low response of the NiO can not be seen in this sample. The response looks essentially identical to the $SrTiO_3$ sample. This is further evidence that the NiO and $SrTiO_3$ are non-reacting.

3.5 Conclusion

Bulk samples of NiO, $SrTiO_3$ and a NiO/$SrTiO_3$ composite have been fabricated from NiO and $SrTiO_3$ powders. Full density was achieved for $SrTiO_3$ however only about 80% density was achieved for NiO. X-ray diffraction data confirms that NiO and $SrTiO_3$ are compatible and non-reacting. FTIR data shows that the $SrTiO_3$ and NiO resonances are at the expected frequencies. It would be useful to obtain permeability and permittivity data from the reflectivity data through analysis such as Kramer-Kronig; however the noise at low frequency makes it very difficult to accurately take the needed integral from zero to infinity. Bulk ceramics would be useful in achieving a negative index in the infrared; however, fabrication processes need to improve to achieve higher density and the FTIR technique could be improved.

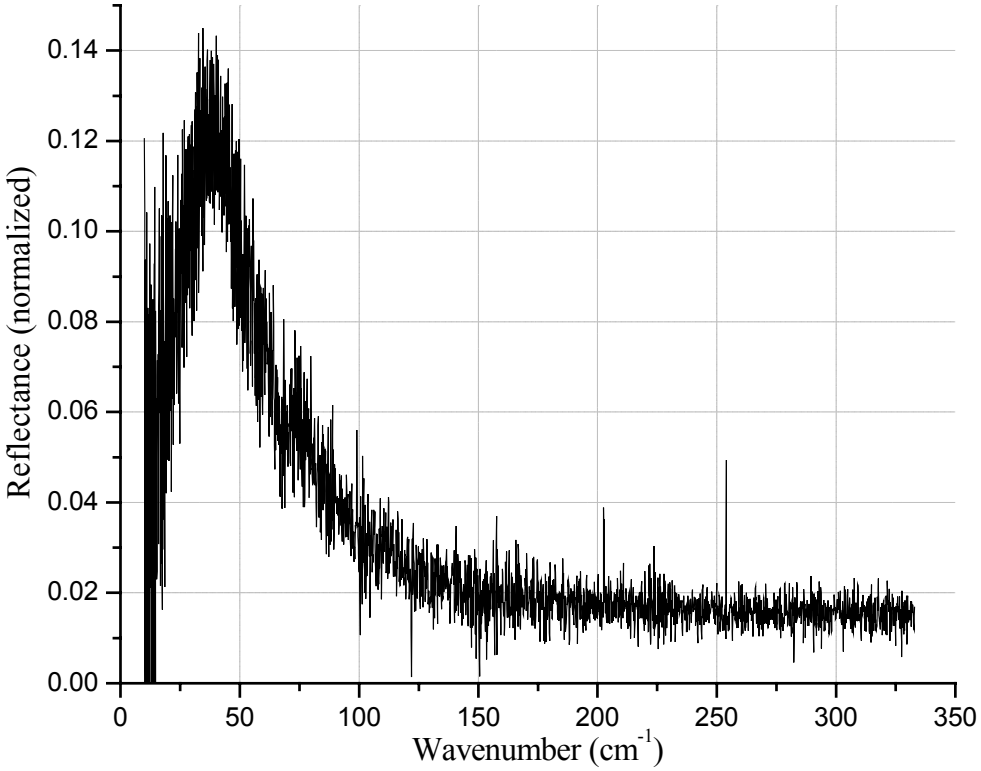

Figure 3.3: FTIR results for a NiO pressed powder sample. The antiferromagnetic resonance peak is clearly seen at about 36 cm^{-1}.

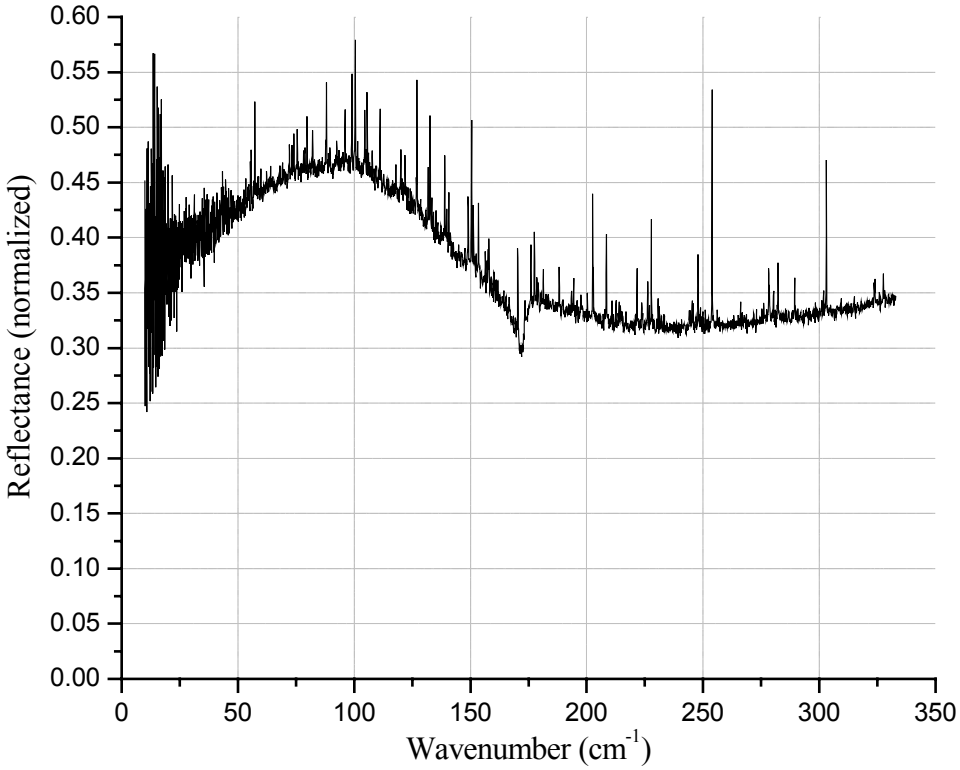

Figure 3.4: FTIR reflectance data for the $SrTiO_3$/NiO composite data. The $SrTiO_3$ ionic resonance is apparent; however the NiO resonance is too weak to see.

CHAPTER 4

THIN FILM DEPOSITION AND ANALYSIS

4.1 Introduction

Another method of obtaining a multiferroic composite is through the use of a thin film heterostructure. Using this method, thin films are layered one on top of another. For THz imaging, the wavelength scale is much larger than the film thickness such that the material will appear to be essentially homogenous although it also lessens the signal response of the film. In order to maximize the signal, it is desirable to achieve single crystal films grown epitaxially.

High quality epitaxy requires that the lattice mismatch between the two materials is small. Lattice mismatch δ is defined as:

$$\delta = \frac{a_\beta - a_\alpha}{a_\alpha} \tag{4.1}$$

The terms a_α and a_β are the lattice parameters of the α and β phases respectively. A small lattice mismatch leads to smaller strain energies at the interface. Epitaxy is typically thought to be reasonable for a lattice mismatch of about 7% or less.

The technique used here is reactive off-axis rf sputtering. With off-axis sputtering, the deposition rate from a given sputtering gun drops as the distance from the gun becomes larger. Figure 4.1 shows the deposition rate for $SrTiO_3$ as a distance from the sputter gun for several rf powers. These rates were measured on a step created by a wax strip on the sample during deposition using profilometry. The varying of deposition rate across a single substrate can be useful for composition spreads[31]. Figure 4.2 shows a schematic of the system used for this work. It has three 90° off-axis sputter guns 90°from each other. Codeposition with two or more of these guns results in a composition spread on a single substrate. The

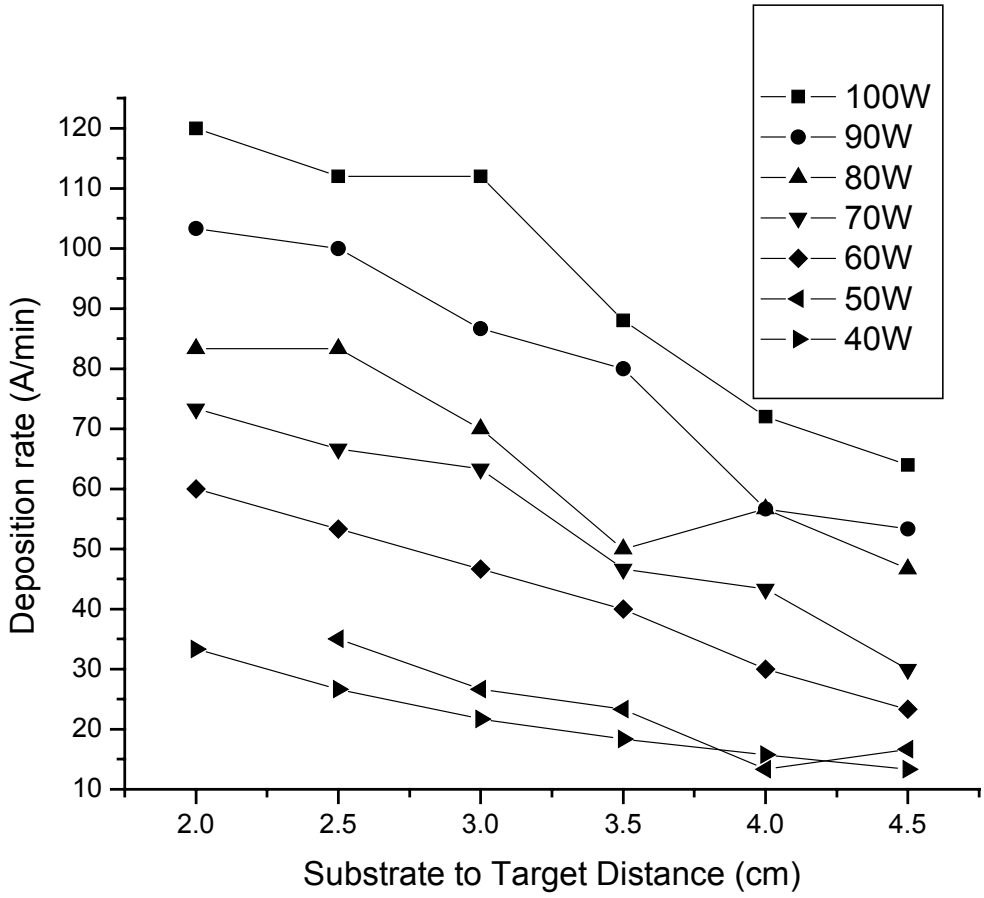

Figure 4.1: Deposition rate for $SrTiO_3$ from a 2 inch US Gun as a function of rf power and substrate to target distance. A few depositions can cover a large range of deposition rate.

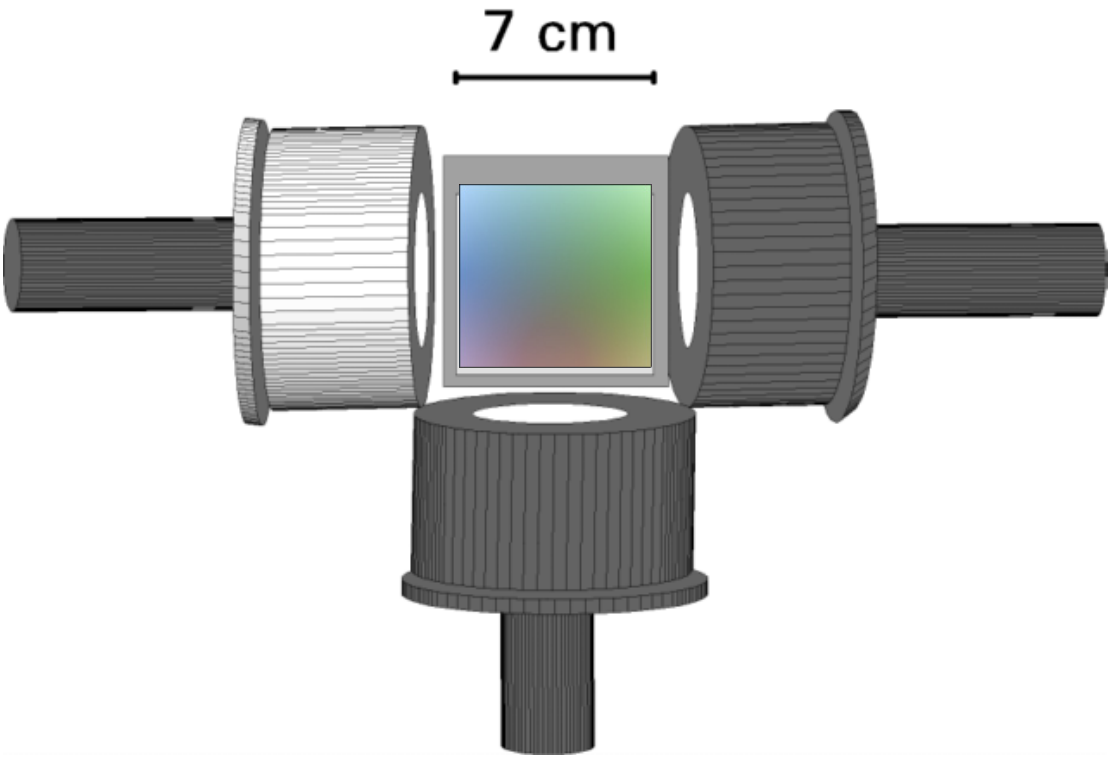

Figure 4.2: Off-axis sputtering system for thin film composition spread technique. Composition at any given location on the substrate depends on the distance from each sputter gun.

composition spread approach will be useful for determining the effect of Ba doping in $SrTiO_3$ and Co or Fe doping in NiO.

In order to achieve epitaxially grown thin films using reactive off-axis rf sputtering, there are several parameters that can be changed. The first of these parameters is the deposition temperature. Raising the temperature increases the surface diffusion that can take place and allow for atoms to move enough to grow epitaxially. The second is changing the deposition rate. This can be accomplished by varying two main parameters. One is by changing the rf power; the other is by changing the target to substrate distance. The pressure and the oxygen partial pressure can also be used to change the rate; however, it can also possibly affect the films chemically and structurally as well. The process parameters for this work varied the substrate temperature from ambient to 600°C, the rf power from 50W to 100W, the deposition pressure was held at 30 mtorr for each deposition. The oxygen partial pressure was changed from 6 mtorr to 12 mtorr.

4.2 X-ray Diffraction Analysis with GADDS

The General Area Detector Diffraction System (GADDS) Bruker AXS uses a two-dimensional detector to achieve a combinatorial approach of examining a range of 2θ and χ[38]. Figure 4.3 shows a schematic of the system. Figure 4.4 shows the output for a polycrystalline corundum sample used as a calibration standard. The sample is polycrystalline and therefore each powder diffraction cone 2θ intersects the two-dimensional detector as a hyperbola. For a single crystal sample, the result will be spots located at the correct geometry. The GADDS system allows for a quick method to locate single crystal diffraction peaks. Pole figures (rotation of ϕ) and rocking curves (vary ω) can be completed to quantify crystal quality.

Another method to quantify crystal quality is to examine the χ dependence on intensity. Figure 4.5 shows the χ dependence of a textured $SrTiO_3$ film. One can take

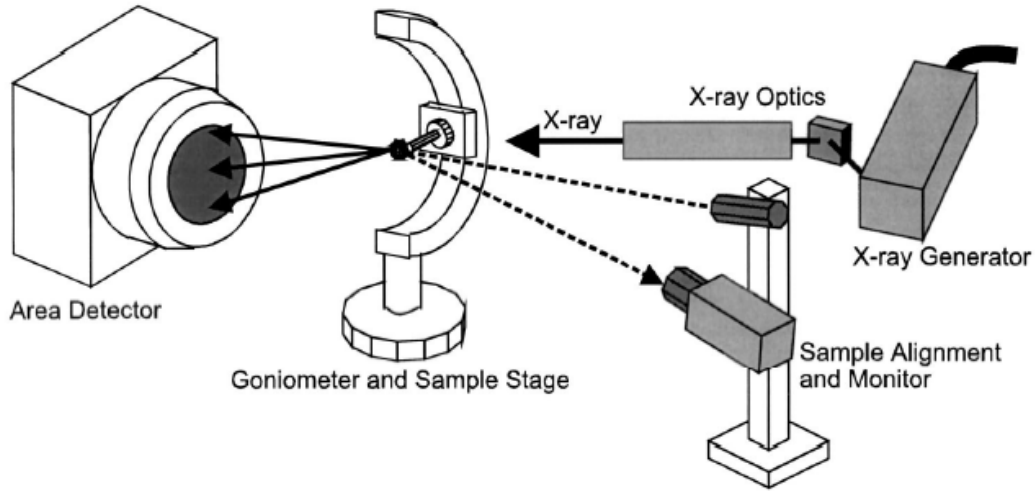

Figure4.3: Schematic of the diffraction with a two-dimensional detector[38]. The geometry can be changed by varying ω, 2θ, χ, and ϕ. The detector collects a range of 2θ and γ.

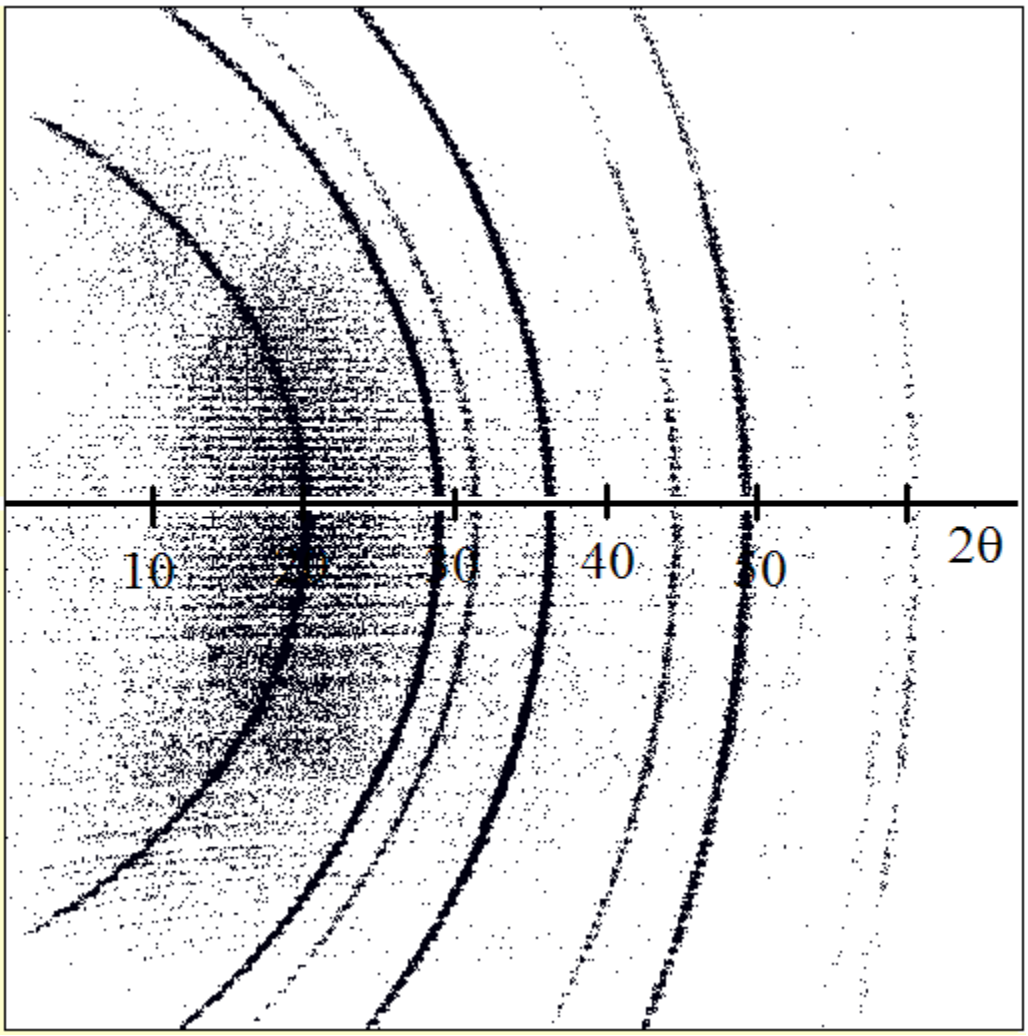

Figure 4.4: GADDS output for a polycrystalline corundum sample used for calibration of equipment. The 2θ scale is shown along the x-axis. χ varies along the curves of equal 2θ which are due to the intersection of the polycrystalline diffraction cone and the two-dimensional detector. $\chi = 90°$ at the x-axis.

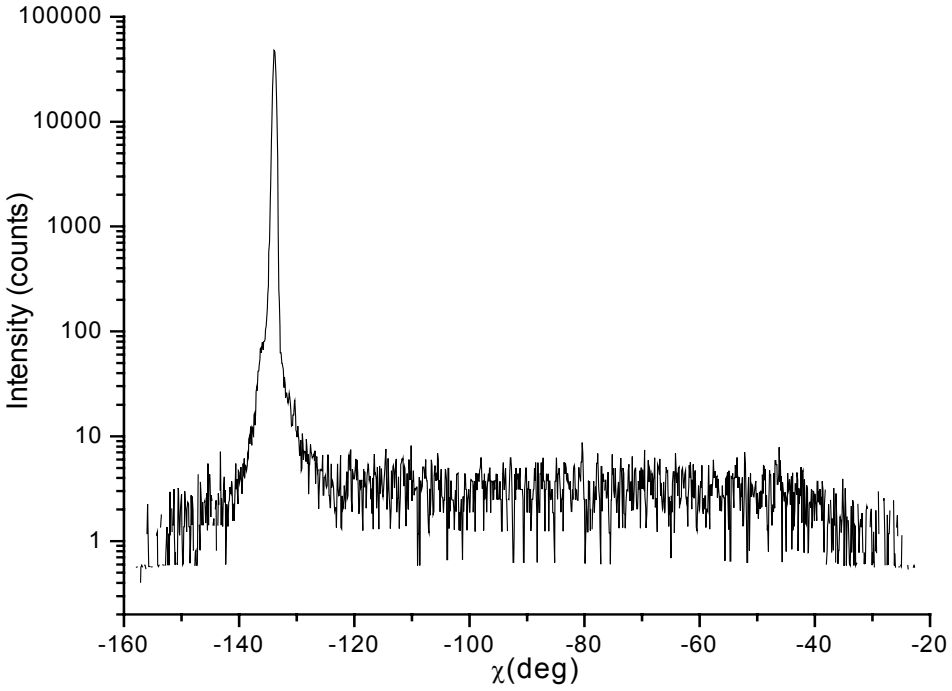

Figure 4.5: Intensity as a function of χ for an epitaxially grown $SrTiO_3$ (110) peak. The single crystal peak gives strong intensity at only a single point in this range of χ. The GADDS allows this method to quickly quantify the level of texturing.

the ratio of the intensity of the epitaxial peak $I(\chi_E)$ to the intensity of the background peak $I(\chi_0)$ to gain information on crystal quality. A polycrystalline sample will have a ratio of 1 or less while a single crystal sample will have a ratio that approaches infinity.

4.3 Rutherford Backscattering: Composition and Crystal Quality

Rutherford baskscattering (RBS) is a standard technique for determining the composition profile of thin films. In this technique, alpha particles are accelerated at the sample with high energy, 1.96 MeV for the present work. The backscattered alpha particles are collected and the resulting energy is measured. The energy of the backscattered particle is proportional to the size of the atom that scattered the particle along with the depth in the material that the alpha particle traveled before backscattering. This results in information on the composition profile as a function of distance. This leads to both composition information and film thickness information. The RBS probe depth is typically 1 μm and allows for a thickness resolution of around 2nm. RBS is capable of detecting atomic fractions down to 10^{-2} to 10^{-5}.

RBS can also be used to analyze single crystal quality. This is accomplished through ion channeling. In single crystals, there are preferred directions which have atoms that are more loosely packed than others. These directions are called channeling directions. When a particle enters a crystal along one of these directions, there is a high probability that it will enter a channel. Inside a channel, most collisions will be grazing type with very little probability of backscattering. This results in a significant decrease in backscattered yield.

Crystal quality can be examined by finding a channeling direction and finding the corresponding decrease in backscattered yield. The ratio of the channeling direction yield to a randomized direction is defined as χ_{min}. The randomized direction

is achieved by rastering the sample through a small angle around both the x and y axis. For high quality single crystals, χ_{min} can be as low as 1 to 5 %[39].

4.4 Multiferroic Thin Film Heterstructure

The goal of this work is to combine $SrTiO_3$ and NiO to make a multiferroic material with a negative index of refraction in the far-infrared. These materials have been shown to be compatible and non-reacting in the form of a bulk ceramic. It is desirable to examine this composite material in thin film form due to several key issues. First, the materials can be grown epitaxially in order to give essentially single crystal properties. Second, the off-axis sputtering allows for the possibility of a composition spread. The composition spread can likely result in many compositions all with excellent crystal quality.

In order to grow films epitaxially, the lattice mismatch must be around 7% or less. NiO has the rocksalt structure with a lattice constant of about 4.17Å. $SrTiO_3$ has the perovskite structure with a lattice constant of 3.91Å. This results in a lattice mismatch of about 6.6% which is reasonable for epitaxial growth. The chosen substrate is single crystal MgO ceramic which has the rocksalt structure with a lattice constant of 4.21Å. This results in less than 1% lattice mismatch with NiO and slightly more than 7% for $SrTiO_3$. These should be compatible for the growth of epitaxially grown multiferroic heterostructure.

4.5 Conclusion

Off-axis sputtering is a good method for the deposition of single crystal thin films. This method allows for future work using composition spreads. XRD and RBS provide two methods of examining the structural properties of the films. RBS can also be used to examine the composition profile and film thickness. $SrTiO_3$ and NiO are expected to be compatible along with a substrate of single crystal MgO for the fabrication of a multiferroic heterostructure.

CHAPTER 5

EPITAXIAL NiO ON MgO SUBSTRATE

5.1 Introduction

In order to achieve an epitaxially grown thin film heterostructure, the first step is to grow the layers individually on the substrate. This is expected to be fairly straight forward for NiO on MgO because both have the rocksalt structure with a lattice mismatch of less than 1%. The closeness of the lattice constant makes for easy epitaxial growth, but makes XRD analysis difficult using GADDS. It is difficult to resolve the NiO diffraction peaks from the strong single crystal substrate peaks. For this reason, RBS channeling is used to verify crystal quality.

5.2 Substrate Preparation

In order to obtain high quality crystalline films, the substrates must be clean and have a defect-free surface. All substrates are first cleaned with acetone followed by an isopropyl alcohol rinse and air dry. In order to maintain good thermal contact between the substrate and heater, silver paste was used as an adhesive. Each substrate was then heated to 90°C for 30 minutes followed by 180°C for 30 minutes to degas the silver paste. The samples were then heated to 600°C under vacuum (base pressure of chamber) for 30 minutes prior to each deposition. This step should remove any water that has adsorbed on the surface of the substrate and give an atomically clean surface.

5.3 Deposition Technique

NiO films were deposited with reactive off-axis rf sputtering using a Ni target in a 2 inch US Gun in an ambient Ar/O_2 gas at 30 mtorr. The rf power used was 100W for all depositions. The oxygen partial pressure was varied from 6 mtorr to 12 mtorr. The substrate was heated to temperatures in the range of room temperature to 600°C. The samples were annealed systematically in air at temperatures ranging from

700°C to 1000°C. The thickness of the films ranged from 1000Å to 4000Å. The resulting deposition rate was about 180Å/min and dropped slightly at the higher oxygen partial pressure.

5.4 XRD Results

It was found that the XRD analysis for single crystal NiO on MgO is difficult using GADDS. This is due to the extremely close lattice match between the two materials. Figure 5.1 shows GADDS output for a NiO/MgO sample centered on the (200) peak. There are three artifacts in the measurement that are immediately noticeable. First, it can be seen that there are streaks that have a direction radial to the location of the strong (200) peak located at approximately 42°. Second, another streak can be seen that has a curvature opposite of the expected for a polycrystalline peak. Third, the (200) peak has a "donut" shape. These are all attributed to the overloading of the detector from the strong substrate peak. The data for Figure 5.1 was taken with a voltage of 20kV and current of 5mA which is much lower than the standard working values of 40kV and 40mA. These artifacts make it difficult to fully analyze the NiO epitaxy on MgO. However, the GADDS detector can still be used to detect the presence of any polycrystalline phases if present as they would be apparent for geometry away from the MgO single crystal peaks.

For the present purposes, the absence of polycrystalline phase implies that there is no film present, the film is completely amorphous or the film has formed with excellent epitaxial quality. The last possibility is confirmed by ion channeling using RBS. For the analysis, the polycrystalline peaks are examined on the shoulder of the MgO (200) peak with omega at approximately 19°. The geometry of the (200) peak is $2\theta \approx 42°$ and therefore an omega of 21°. It should also be noted that no other phases other than NiO have been seen on any sample which is evidence that the Ni is fully oxidized in the entire range of oxygen partial pressure examined.

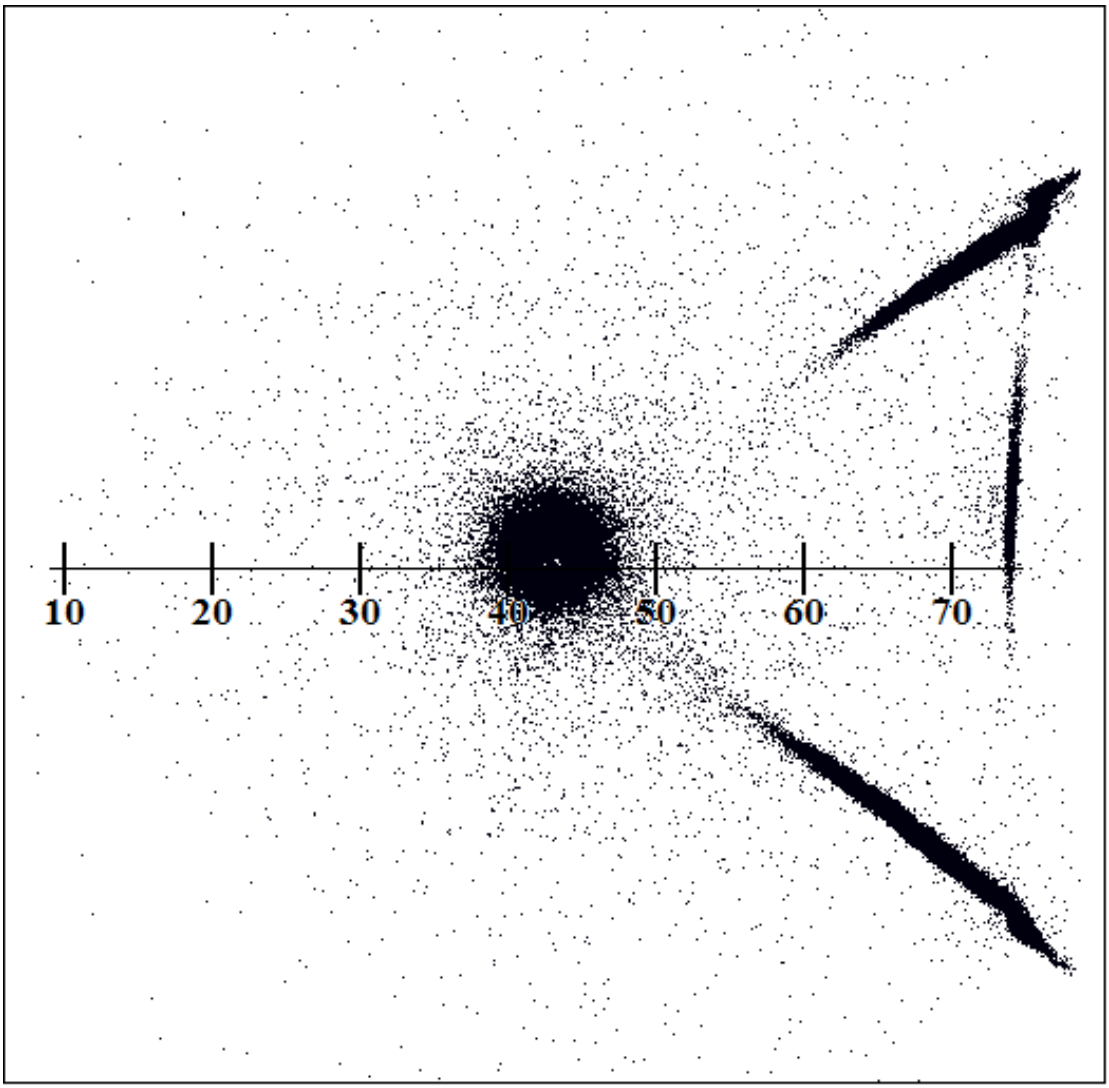

Figure 5.1: GADDS output for a NiO/MgO sample centered on the (200) peak for NiO. The substrate peak is at essentially the same geometry and the strong peak overloads the detector resulting in incorrect counts in several locations. This data was taken with a source of 20kV and 5mA, which is much lower than the standard values of 40kV and 40mA. It is not possible to resolve the smaller NiO peak.

Figure 5.2 shows the GADDS output for four samples deposited at various substrate temperatures. It can be seen that there is significant texture of the thin film even at a substrate temperature of 200°C as seen by spots along the hyperbola. As the substrate temperature increases, the crystal orientation improves. At a substrate temperature of 600°C, there is no evidence of non-epitaxially oriented grains seen as an absence of hyperbola.

It has also been found that annealing at high temperature in air improves crystal quality. Figure 5.3 shows the GADDS results for a sample deposited at 300°C before and after annealing at 700°C in air for 1 hour. The polycrystalline peaks are very faint after annealing showing that the film is mostly epitaxially oriented. For a sample deposited at 200°C, improvement was seen however, significant polycrystalline phase remains even after annealing at 1000°C.

5.5 Ion Channeling with RBS

Ion channeling using RBS has been completed to verify the epitaxy quality of the NiO thin films grown on MgO substrates. Figure 5.4 shows the channeling results for a sample deposited at 600°C. The RBS acceleration voltage was 1.96 MeV and the current was approximately 11nA. The dose used was 10μC. The film thickness was found to be about 3500Å and comparison with simulation suggests that the NiO is fully oxidized. The channeling direction used was the [100] direction. The random direction was taken while rastering through a few degrees about the x and y axes. The resulting χ_{min} is approximately 7%. This is very strong evidence that the NiO has been deposited with excellent crystal quality.

5.6 Conclusion

It has been shown that NiO grows epitaxially very easily on MgO substrates using reactive off-axis rf sputtering. NiO grows with a strongly preferred orientation

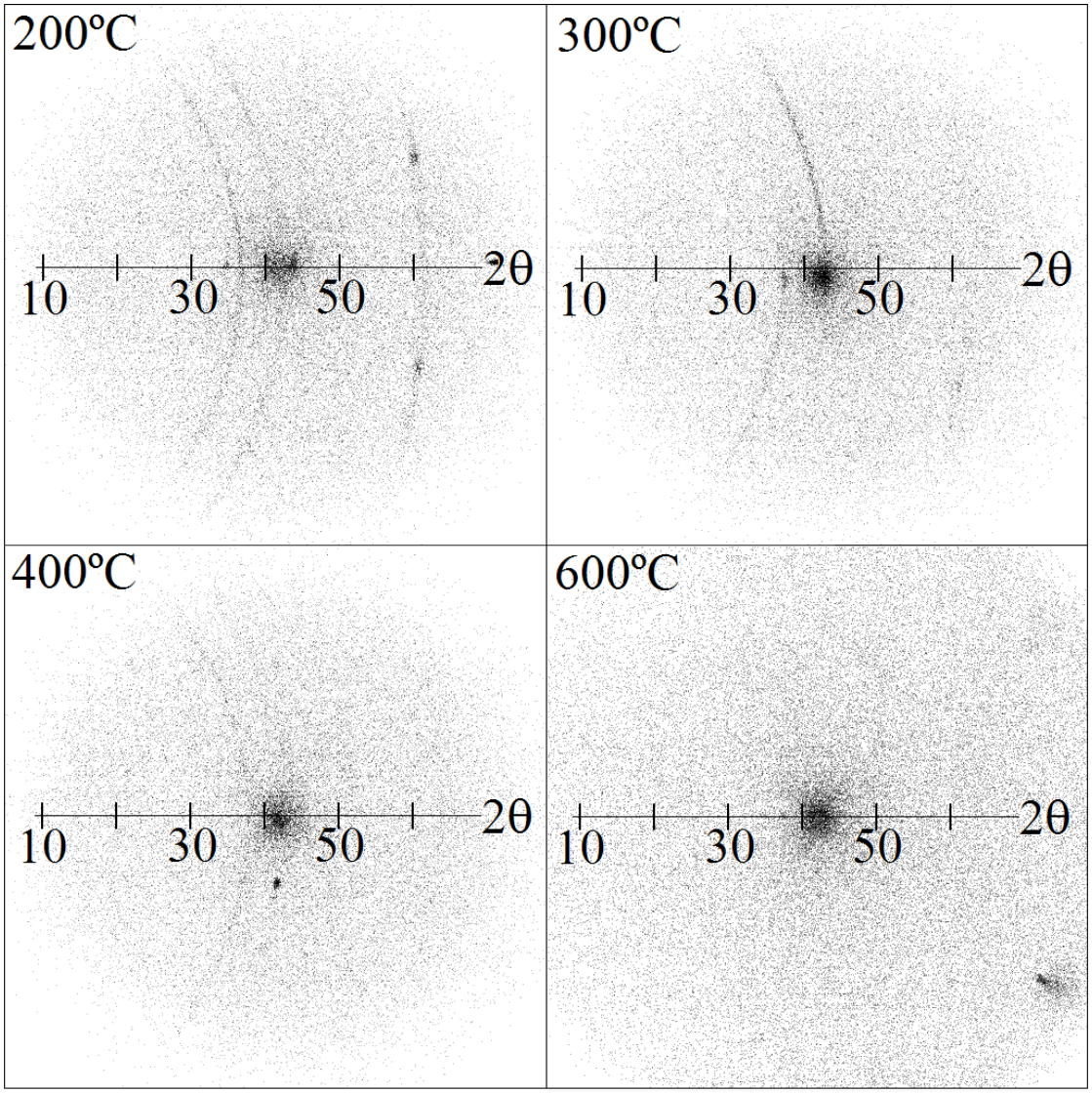

Figure 5.2: GADDS output for NiO/MgO samples deposited at various temperature on the shoulder of the NiO/MgO (200) peak. Polycrystalline arcs are clearly seen at 200°C with some evidence of texturing. With a substrate temperature of 600°C, there is no evidence of misoriented phase.

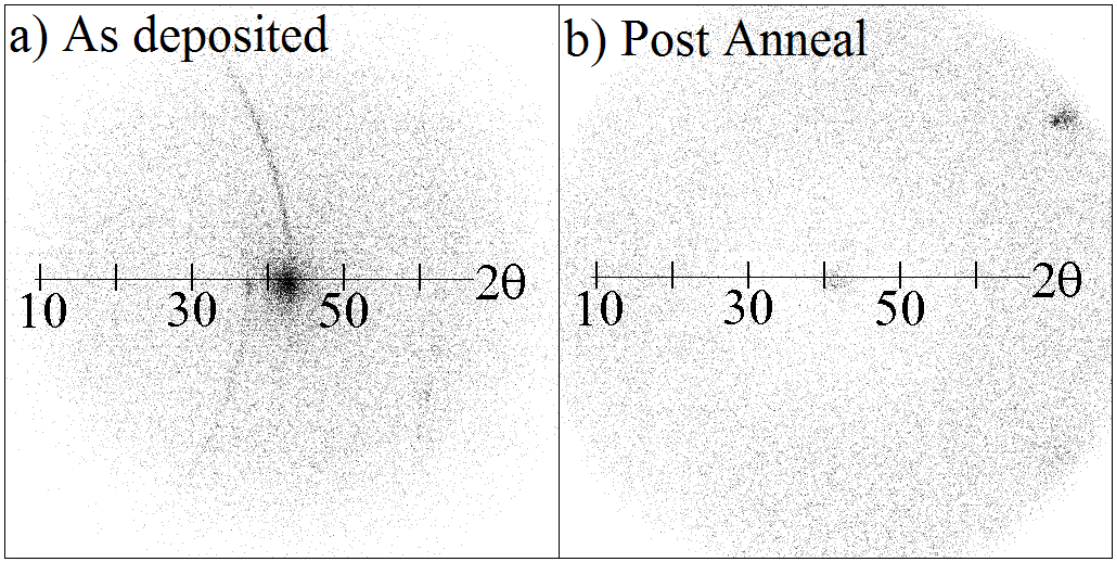

Figure 5.3: GADDS output for a NiO/MgO sample deposited at 300°C as deposited and after annealing at 1000°C for 1 hour in air. There is no evidence of misoriented phase after annealing.

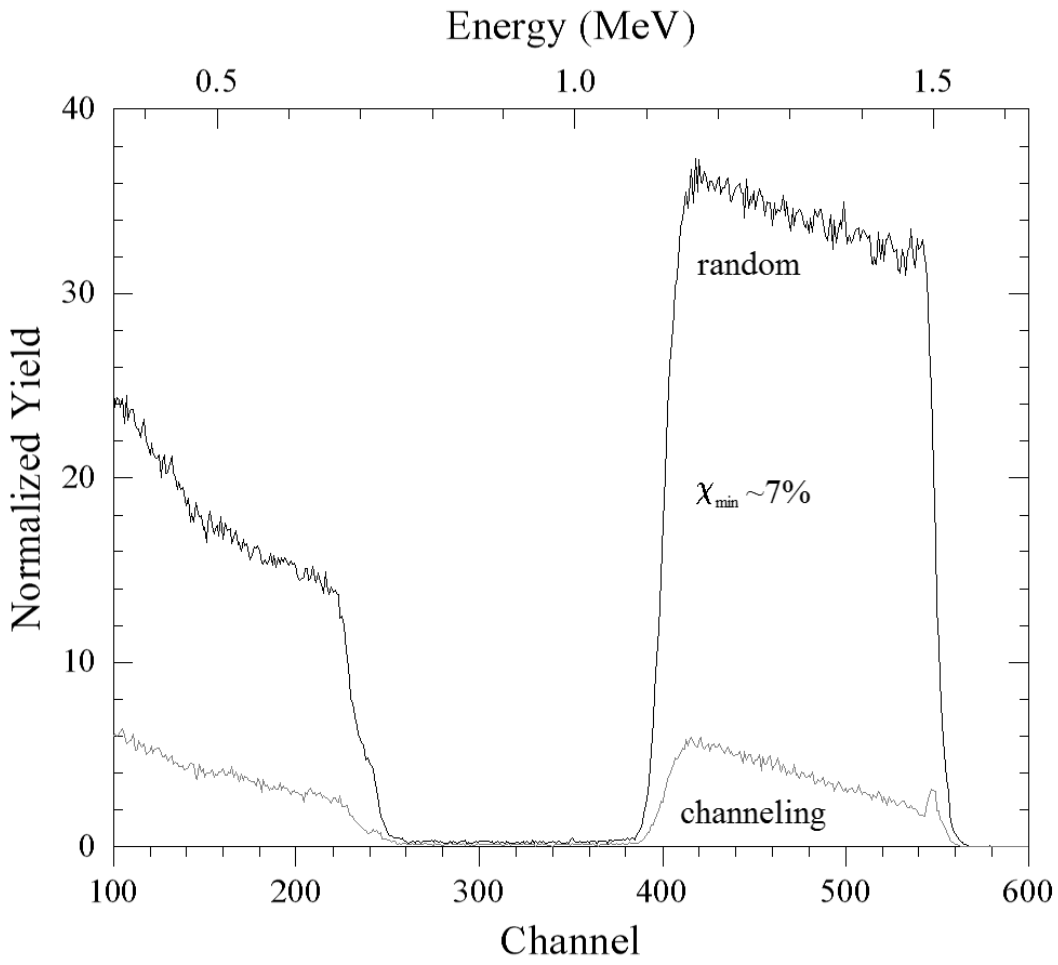

Figure 5.4: Ion channeling with RBS for a NiO/MgO sample deposited at 600°C. The backscattered yield drops to around 7% for a channeling direction over a random direction taken by rastering the sample. This is strong evidence that the NiO has grown with excellent crystal quality.

at a substrate temperature as low as 200°C and a deposition rate of around 180Å/min. High quality epitaxial films are achieved for deposition temperatures at or above 600°C for this deposition rate. High quality epitaxy can also be achieved by depositing at a temperature of 300°C or above followed by annealing at 700°C in air for an hour. The absence of polycrystalline phase was verified using XRD and epitaxy quality has been verified using ion channeling with RBS.

CHAPTER 6

EPITAXIAL $SrTiO_3$ ON MgO SUBSTRATE

6.1 Introduction

The next step in achieving a heterostructure of NiO and $SrTiO_3$ on MgO is to grow $SrTiO_3$ on the MgO substrate. $SrTiO_3$ has the perovskite structure with a lattice constant of 3.91Å with a lattice mismatch of approximately 7% to the MgO substrate. This large mismatch makes growth of an epitaxial film more difficult than for NiO on MgO. It is expected that high temperatures are needed to achieve the surface mobility needed to grow epitaxial with such a high mismatch.

6.2 Deposition Technique

The substrates were prepared using the procedure outlined in Chapter 5. The films were deposited by r. f. reactive off-axis sputtering using a stoichiometric $SrTiO_3$ target in a 2 inch US Gun in and Ar/O_2 gas at 30 mtorr. The oxygen partial pressure was varied from 6 mtorr to 12 mtorr. The r. f. power was ranged from 40 to 100W. The substrate to target distance was varied from 2 to 5 cm. These parameters resulted in a deposition rate that varied from about 20 Å/min to 120 Å/min. The target thickness was 2000 Å for each sample.

6.3 XRD Results

The crystal structure of $SrTiO_3$ allows for more complete XRD analysis than for NiO when grown on a single crystal MgO substrate. The perovskite structure allows for several strong diffraction peaks that are forbidden for the MgO rocksalt structure. The {100} and {110} diffraction peaks are strong for $SrTiO_3$ but are forbidden for MgO. The {100} peaks allow for rocking curves using the GADDS while the {110} peaks can be used for pole figures. This results in analysis of in plane and out of plane orientation.

In order to determine the effect of processing parameters on the structure chi dependence of the (110) peak was analyzed using the chi intensity ratio described in Chapter 4. It was first found it was not possible to achieve epitaxy with standard processing r. f. power of 100W for the 2 inch target even with a temperature of 600°C. This temperature is the highest that the system used could achieve. The next step was to lower the deposition rate by lowering the r. f. power and increasing the substrate-to-target distance. For this experiment, the temperature was held at 600°C for all depositions. Figure 6.1 shows the effect of the chi ratio as a function of deposition rate for these samples. It can be seen that there is a sharp increase in crystal quality when the deposition rate decreases below about 30Å/min. It is expected that deposition parameters of 50W, 40% O_2 in Ar at 30 mtorr and a substrate to target distance of 2.5cm should allow for epitaxially grown films with a deposition rate slightly under 30 Å/min.

The next step is to determine the effect of high temperature annealing on crystal quality. Table 6.1 summarizes the effect of annealing on the FWHM of the (100) rocking curve and the χ ratio of the (110) peak. Each anneal was done in air for 1 hour on the same sample. The FWHM of the rocking curve was found by using a Lorenztian fit of the experimental data. It can be seen that there is reasonable crystal quality of the as deposited film which improves greatly upon annealing. It appears that in both of these measures of crystal quality that the 1000°C anneal resulted in the best crystal quality. This resulted in a rocking curve width of 0.32° which suggests excellent crystal quality.

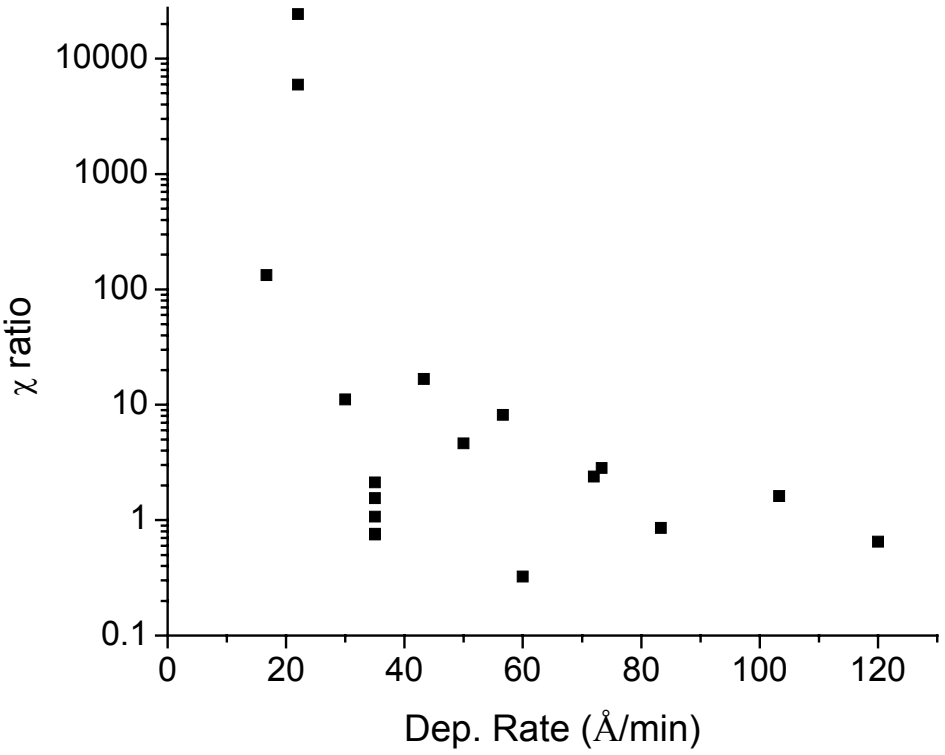

Figure 6.1: Effect of the crystal quality of $SrTiO_3$ as measured by the χ ratio on deposition rate. Crystal quality improves dramatically after the deposition rate decreases below 30Å/min.

Table 6.1: Effect of annealing temperature on crystal quality of $SrTiO_3$ by measuring the FWHM of a (100) rocking curve and the χ ratio of the (110) diffraction peak.

Annealing Temp (°C)	FWHM of ω in °	Intensity ratio of χ
No Anneal	0.44	1800
800°C	0.38	4973
1000°C	0.32	5365
1200°C	0.38	1379

From Table 6.1, it is expected that a 1000°C anneal results in the highest crystal quality. A second sample was annealed at 1000°C in air for 1 hour to verify that a single anneal is sufficient to achieve high crystal quality. Figure 6.2 shows the (100) rocking curve along with the (110) ϕ plot for this sample. The ϕ plot is from the post anneal measure. It is first seen that this film has a wider FWHM than the sample of Table 6.1. This is likely due to substrate differences. The two samples were on substrates from two different manufacturers. It is noticeable that annealing at 1000°C for 1 hour greatly improves the crystal quality. The ϕ plot also shows evidence of excellent four fold symmetry which is expected for rotation around the [001] axis. These data are strong evidence that the $SrTiO_3$ film has been grown on MgO with excellent epitaxial crystal quality.

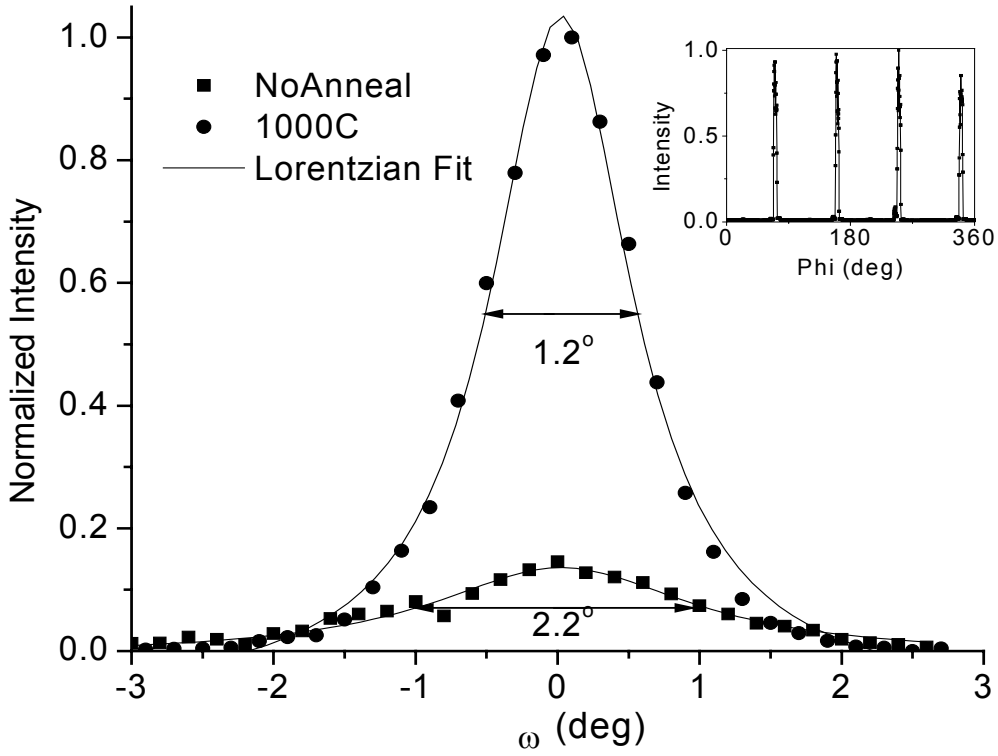

Figure 6.2: $SrTiO_3$ (100) rocking curve and (110) ϕ dependency for a sample deposited at 600°C and annealed at 1000°C. The rocking curve is narrow and the ϕ plot shows excellent four-fold symmetry.

6.4 RBS Results

RBS was used to verify the chemical composition profile of the $SrTiO_3$ films along with film thickness. The RBS profiles were compared to simulations by RUMP software by Genplot. Figure 6.3 shows the RBS results for a sample deposited at 600°C and annealed at 1000°C for 1 hour in air. This samples shows that the $SrTiO_3$ has been deposited stoichiometrically and is about 3300 Å thick suggesting a deposition rate of about 70 Å/min. There is about 1% Ba that was discovered in the film. This is likely contamination that resulted from the $SrTiO_3$ target being used for (Ba, Sr)TiO_3 codeposition composition spreads completed in the same chamber. This is not expected to be a serious problem in that Ba doping is likely to be needed in order to shift the $SrTiO_3$ ionic resonance frequency.

There have been reports of Mg diffusion into thin films out of MgO substrates[40]. This appears to be a minor problem with $SrTiO_3$ grown on MgO. For the sample of Figure 6.4, simulation shows that there is a layer of "fuzzing" in which a small amount of interdiffusion between the MgO substrate and the $SrTiO_3$ film. This layer is approximately 500 Å in depth. This appears to be the case in all samples examined. It is unclear what the effect of Mg in the $SrTiO_3$ will have on the dielectric properties.

One sample showed an anomalous Mg contamination. This sample was deposited at 600°C at 100W power and 20% O_2 in Ar, corresponding to a deposition rate of about 130 Å/min. The RBS results are shown in Figure 6.4. This sample shows an interesting region at the top surface of the $SrTiO_3$ film that has a large amount of Mg. This region is about a 1000Å thick. There is again a "fuzzing" layer between the two films as well. This interesting result has not been explained to date and all attempts to reproduce this have failed. This type of Mg contamination is not common however; it would be extremely detrimental to any thin film.

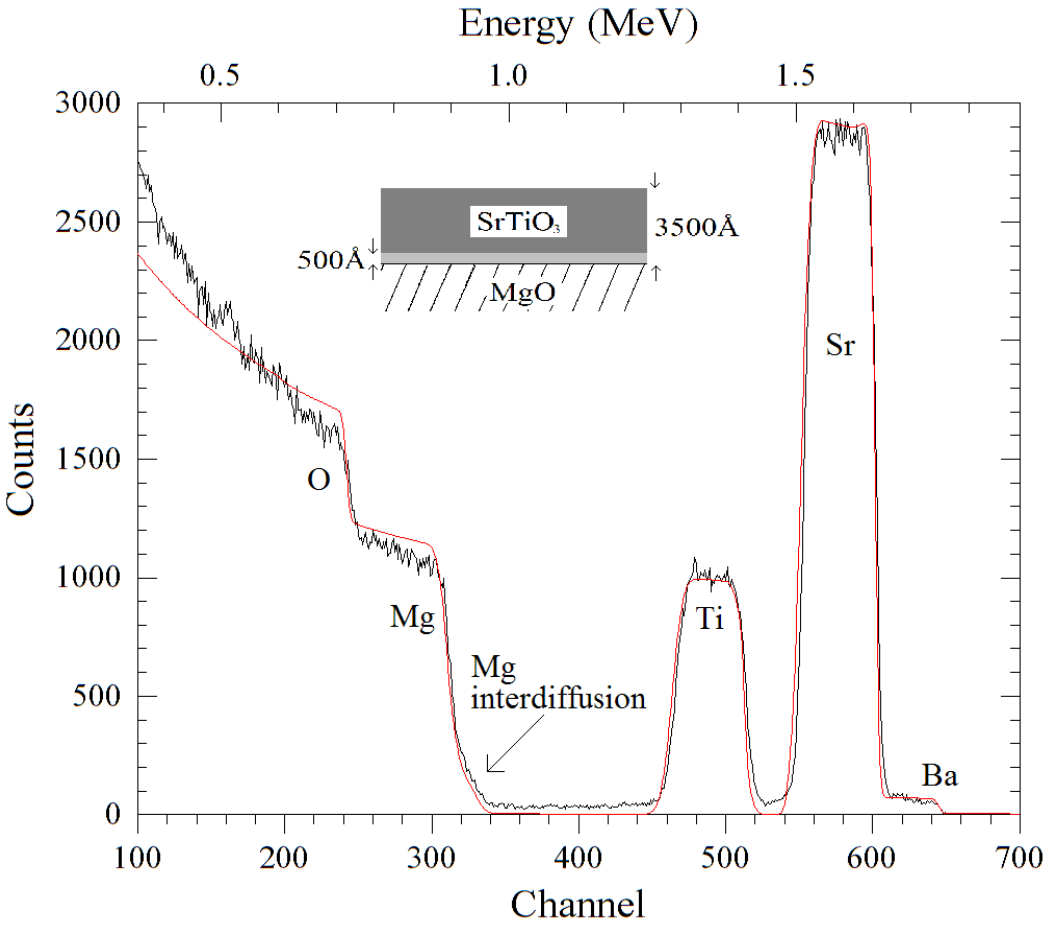

Figure 6.3: RBS output for 3500Å $SrTiO_3$ on MgO. A 500Å interdiffusion layer is required in order for simulation to match with experiment. The small amount of Ba (less than 1%) is attributed to contamination in the ceramic target.

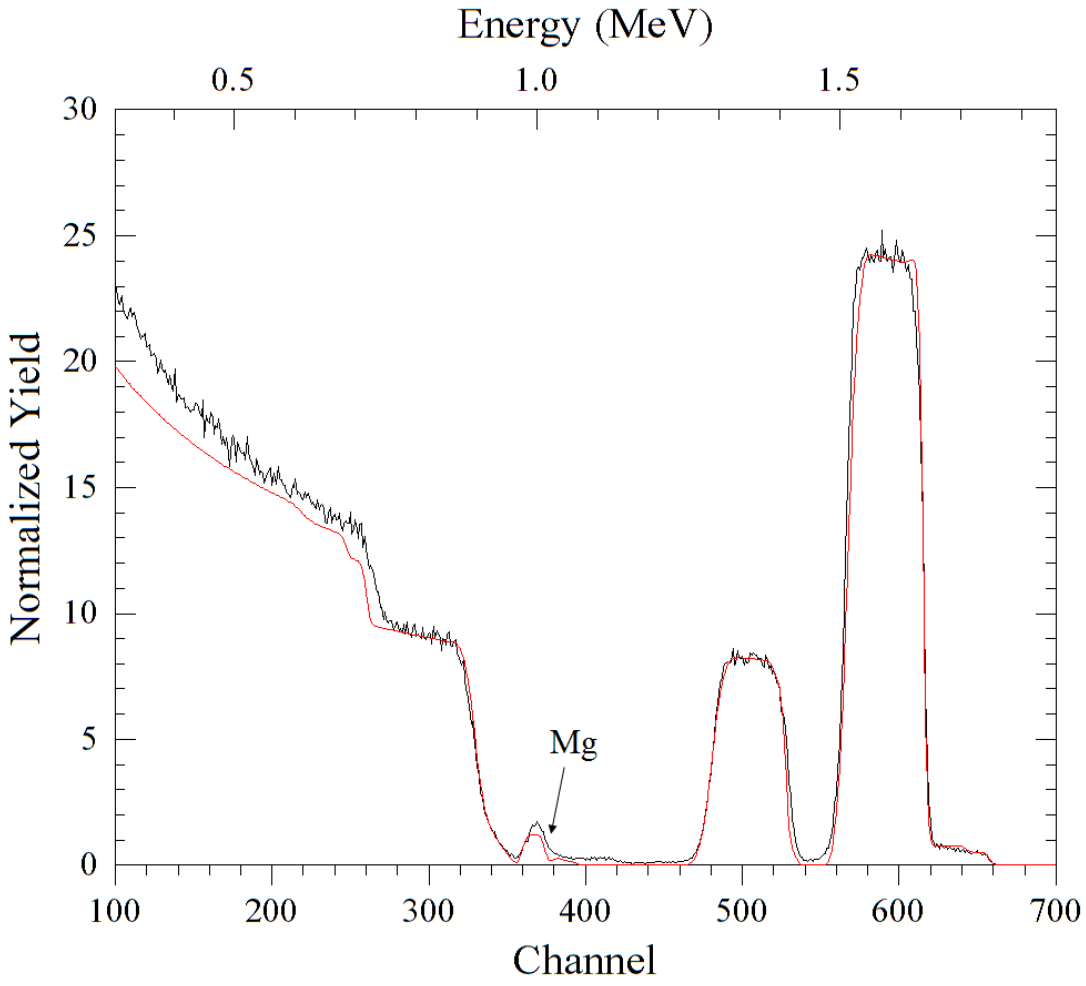

Figure 6.4 RBS output that shows anomalous Mg diffusion. A large amount of Mg is seen in the top 1000Å of the film. The bottom fuzzing layer is still required to fit to simulation.

6.5 Conclusion

Single crystal thin films of $SrTiO_3$ have been grown on MgO substrates using reactive off-axis r. f. sputtering. High temperature and a low deposition rate are needed in order to grow films with high quality epitaxy. A high temperature anneal of 1000°C greatly increases the crystal quality of the as deposited film. Increasing the annealing temperature does not improve the crystal quality and increases the likelihood of Mg contamination. RBS shows that there is some level of Mg contamination in all films with the possibility of gross contamination. In conclusion, high quality single crystal films of $SrTiO_3$ have been grown on MgO substrates that should exhibit excellent dielectric properties.

CHAPTER 7

$(SrTiO_3/NiO)_n$/MgO EPITAXIAL THIN FILM HETEROSTRUCTURE

7.1 Introduction

High quality epitaxial thin films of NiO and $SrTiO_3$ have been grown on MgO substrates using reactive off-axis rf sputtering. The next step is to create an epitaxially grown $(SrTiO_3/NiO)_n$/MgO heterostructure. It should be fairly straightforward to grow $SrTiO_3$ on NiO due to the similarity of lattice between NiO and MgO and the extremely high crystal quality of the NiO achieved on as grown films. The slight difference in lattice constant between NiO and MgO should actually aid in the growth of epitaxial $SrTiO_3$. It should also be possible to do the reverse and grow NiO on epitaxial $SrTiO_3$.

In order to create the heterstructure, it is desirable to deposit the second film immediately sequential to the first without breaking vacuum or changing process parameters. The deposition temperature chosen is 600°C. This temperature allows for $SrTiO_3$ epitaxy and high quality NiO without annealing. The chamber pressure was held at 30 mtorr with an oxygen partial pressure of 12 mtorr balance argon. The NiO was again deposited from an elemental Ni target at 100W while the $SrTiO_3$ was deposited from a stoichiometric $SrTiO_3$ target with a power of 50W. The target thickness for each layer was 2000Å.

7.2 Results and Analysis

The first structure to examine is the $SrTiO_3$/NiO/MgO heterostructure. This is expected to be a straightforward extension to the previously grown films and is not expected to require major changes to achieve high quality films. The crystal quality of this heterostructure can also be easily verified since the top film has strong peaks that are not hidden by the substrate. Figure 7.1 shows the $SrTiO_3$ (100) rocking curve and

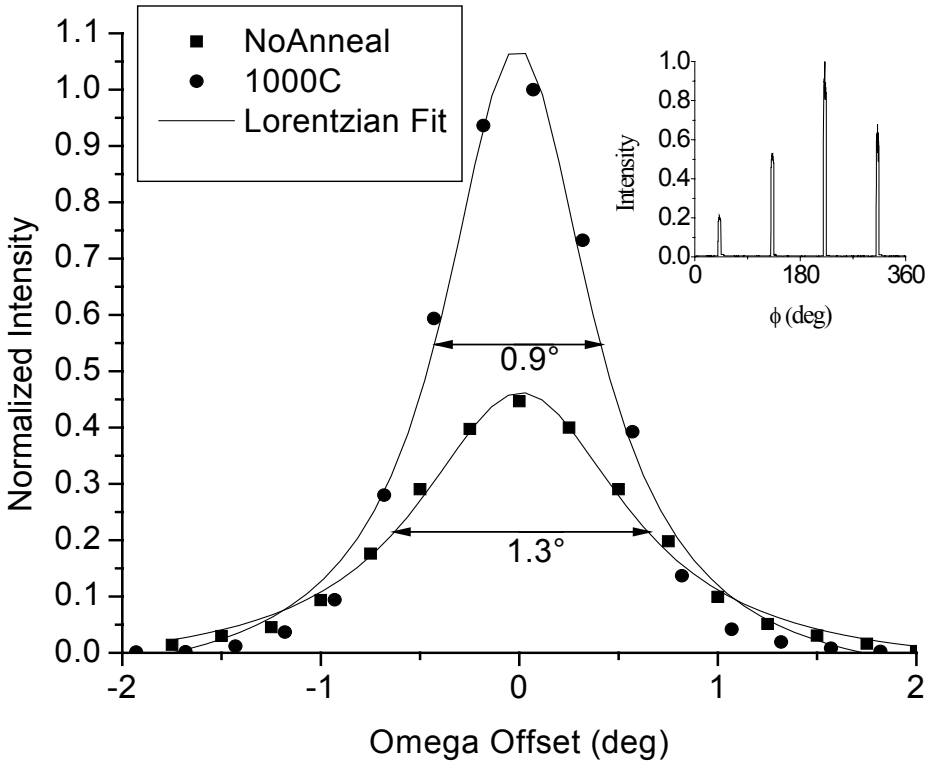

Figure 7.1: $SrTiO_3$ (100) rocking curve and (110) ϕ plot for a $SrTiO_3$/NiO/MgO sample. Data show a narrow rocking curve and reasonable four-fold symmetry in the ϕ plot.

the $SrTiO_3$ (110) pole figure for this heterostructure after annealing at 1000°C for 1 hour in air. The FWHM for this rocking curve is 0.9° which is actually an improvement over the $SrTiO_3$/MgO case. The pole figure also shows reasonable four fold symmetry.

The second structure formed was the opposite stack of NiO/$SrTiO_3$/MgO. This stack was formed with the same process parameters as stated above. It was found that this structure exhibited reasonable crystal quality for $SrTiO_3$ and a small amount of misoriented NiO. The crystal quality of this structure appears to be reasonable.

The final structure fabricated and the most practical is the heterostructure $(SrTiO_3/NiO)_n$/MgO with n = 2. This stack resulted in high crystal quality with only minor decreasing in crystal quality from the single stack. Figure 7.2 shows the $SrTiO_3$ (100) rocking curve and (110) pole figure for this sample. The FWHM for this rocking curve has increased to 1.9° which is very reasonable for a large heteroepitaxial stack. This crystal quality should result in excellent magnetic and dielectric properties for the composite material.

7.3 Conclusion

A thin film heterostructure of antiferromagnetic NiO and dielectric $SrTiO_3$ has been fabricated with excellent crystal quality. XRD analysis has shown that the $(SrTiO_3/NiO)_2$/MgO heterostructure has been grown with excellent crystal quality. These structures should have excellent magnetic and dielectric properties that should be useful for work towards achieving a negative index of refraction in the far infrared.

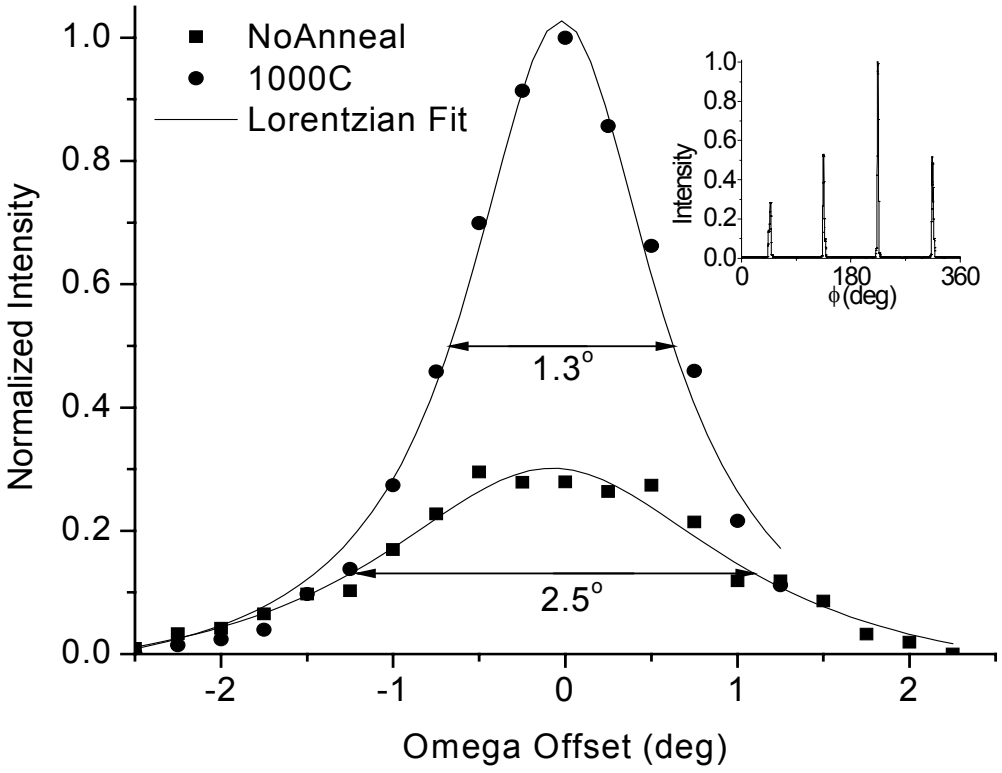

Figure 7.2: $SrTiO_3$ (100) rocking curve and (110) ϕ plot for a $(SrTiO_3/NiO)_n/MgO$ sample. Data show a narrow rocking curve and reasonable four-fold symmetry in the ϕ plot.

CHAPTER 8

CONCLUSIONS

It has been shown that a material that has both a negative permeability and a negative permittivity at the same frequency results in a negative index of refraction at that frequency. It has been proposed that it should be possible to achieve this effect using only intrinsic material properties. Negative permeability and negative permittivity are often associated with resonance frequencies. If an intrinsic magnetic resonance is matched to an intrinsic dielectric resonance at the same frequency, it is possible that the material will exhibit a negative index of refraction. Antiferromagnetic resonances and ionic resonances in many dielectrics tend to occur at frequencies in the far infrared near the same frequency. Therefore, it should be possible to engineer a material that matches an antiferromagnetic resonance with an ionic resonance to achieve a negative index in the far infrared.

It is proposed that antiferromagnetic NiO and dielectric $SrTiO_3$ should have resonances that could be engineered to match. The NiO resonance is at about 36 cm^{-1} and should shift to higher frequency with an applied magnetic field or by doping with a high anisotropy ion such as Fe^{2+} or Co^{2+}. The $SrTiO_3$ ionic resonance is located at about 100 cm^{-1} and should decrease in frequency upon cooling or with Ba doping, which raises the ferroelectric Curie temperature. A combination of these methods should allow for a negative index of refraction to be engineered in a composite material of NiO and $SrTiO_3$.

Bulk ceramic processing was used to verify that NiO and $SrTiO_3$ are compatible and non-reacting. XRD data showed that a pressed powder composite of NiO/$SrTiO_3$ has only rocksalt NiO and perovskite $SrTiO_3$ phases apparent. No

significant shift in d spacing was realized. FTIR measurements verified the existence of the resonances of NiO and $SrTiO_3$ in bulk powder form.

Thin film heterostructures of NiO and $SrTiO_3$ have also been grown on MgO single crystal substrates. These films have been shown to have excellent crystal quality which should result in excellent magnetic and dielectric properties. This heterostructure can be used in the future to quickly determine the correct doping levels needed using composition spreads. In order to measure the high frequency response of these materials, better FTIR equipment is needed to achieve a reasonable signal to noise ratio. It is likely that this can be done using polarized radiation and higher intensity radiation such as from a synchrotron source.

It is proposed that an engineered composite material of NiO and $SrTiO_3$ can result in a negative index of refraction in the far infrared. These materials have been shown to be non-reacting up to temperatures of 1550°C and have been shown to be compatible for epitaxially grown thin film heterostructures. It should be possible to engineer these composite materials such that a negative index of refraction results.

REFERENCES

[1]M. Fiebig, Journal of Physics D: Applied Physics **38,** 123-152 (2005).

[2]V. E. Wood and A. E. Austin, International Journal of Magnetism **5,** 303-15 (1974)

[3]D. N. Astrov, Soviet Physics -- JETP **13,** 729-733 (1961).

[4]R. E. Cohen, Nature **358,** 136-138 (1992).

[5]N. A. Hill, Journal of Physical Chemistry B **104,** 6694-6709 (2000).

[6]N. Hill and A. Filippetti, Journal of Magnetism and Magnetic Materials **242-245,** 976-979 (2002).

[7]L. Fuentes, M. Garcia, J. Matutes-Aquino, and D. Rios-Jara, Journal of Alloys and Compounds **369,** 10-13 (2004).

[8]G. Liu, C.-W. Nan, N. Cai, and Y. Lin, Journal of Applied Physics **95,** 2660-2664 (2004).

[9]J. Wang, J. B. Neaton, H. Zheng, V. Nagarajan, S. B. Ogale, B. Liu, D. Viehland, V. Vaithyanathan, D. G. Schlom, U. V. Waghmare, N. A. Spaldin, K. M. Rabe, M. Wuttig, and R. Ramesh, Science **299,** 1719-1722 (2003).

[10]J. Zhai, N. Cai, Z. Shi, Y. Lin, and C.-W. Nan, Journal of Applied Physics **95,** 5685-5690 (2004).

[11]K.-S. Chang, M. A. Aronova, C.-L. Lin, M. Murakami, M.-H. Yu, J. Hattrick-Simpers, O. O. Famodu, S. Y. Lee, R. Ramesh, M. Wuttig, I. Takeuchi, C. Gao, and L. A. Bendersky, Applied Physics Letters **84,** 3091-3093 (2004).

[12]J. van Suchtelen, Philips Res. Rep. **27,** 28-37 (1972).

[13]J. Ryu, A. V. Carazo, K. Uchino, and H.-E. Kim, Japanese Journal of Applied Physics, Part 1: Regular Papers and Short Notes and Review Papers **40,** 4948-4951 (2001).

[14]D. T. Margulies, F. T. Parker, and A. E. Berkowitz, in *Magnetic anomalies in single crystal Fe[sub 3]O[sub 4] thin films*, Minneapolis, Minnesota (USA), 1994 (AIP), p. 6097-6099.

[15]S. Venzke, R. B. vanDover, J. M. Phillips, E. M. Gyory, T. Siegrist, C.-H. Chen, D. Werder, R. M. Fleming, R. J. Felder, E. Coleman, and R. Opila, Journal of Materials Research **11,** 1187-1198 (1996).

[16]H. Zheng, J. Wang, S. E. Lofland, Z. Ma, L. Mohaddes-Ardabili, T. Zhao, L. Salamanca-Riba, S. R. Shinde, S. B. Ogale, F. Bai, D. Viehland, Y. Jia, D. G. Schlom, M. Wuttig, A. Roytburd, and R. Ramesh, Science **303,** 661-663 (2004).

[17]Feynman

[18]V. G. Veselago, Soviet Physics Uspekhi **10,** 509 (1968).

[19]R. W. Ziolkowski and A. D. Kipple, IEEE Transactions on Antennas and Propagation **51,** 2626-2640 (2003).

[20]C. M. Krowne, IEEE Transactions on Microwave Theory and Techniques **51,** 2269-2283 (2003).

[21]J. B. Pendry, Optics Express **11,** 755-760 (2003).

[22]J. B. Pendry and S. A. Ramakrishna, Physica B: Condensed Matter **338,** 329-332 (2003).

[23]J. B. Pendry and D. R. Smith, Physics Today **57,** 37-43 (2004).

[24]R. A. Shelby, D. R. Smith, and S. Schultz, Science **292,** 77-79 (2001).

[25]M. Notomi, Physical Review B **62,** 10696-10705 (2000).

[26]D. R. Fredkin and A. Ron, Applied Physics Letters **81,** 1753-1755 (2002).

[27]A. Alu and N. Engheta, IEEE Transactions on Antennas and Propagation **51,** 2258-2271 (2003).

[28]A. S. Barker and M. Tinkham, Physical Review **125,** 1527 (1962).

[29]C. Kittel, *Introduction to Solid State Physics*, 3rd ed. (John Wiley & Sons, New York, 1966).

[30]M. R. Daniel and A. P. Cracknell, Physical Review **177,** 932-941 (1968).

[31]R. B. Van Dover and L. F. Schneemeyer, Macromolecular Rapid Communications **25,** 150-157 (2004).

[32]W. Cochran, Advances in Physics **9,** 387-423 (1960).

[33]A. S. Barker, in *Ferroelectrics*, edited by E. F. Weller (Elsevier Publishing Company, Amsterdam-London-New York, 1967), p. 213-250.

[34]R. A. Cowley, Physical Review **134,** A981-A997 (1964).

[35]S. S. A. Seo, H. N. Lee, and T. W. Noh, Thin Solid Films **486,** 94-97 (2005).

[36]J. T. Last, Physical Review **105,** 1740-1750 (1957).

[37]W. G. Spitzer, R. C. Miller, D. A. Kleinman, and L. E. Howarth, Physical Review **126,** 1710-1721 (1962).

[38]B. B. He, Powder Diffraction **18,** 71-85 (2003).

[39]L. C. Feldman, J. W. Mayer, and S. T. Picraux, *Materials Analysis by Ion Channeling* (Academic Press, Inc., New York, NY, 1982).

[40]X. Yao, K. Nomura, M. Yoshizumi, M. Kuznetsov, Y. Nakamura, T. Izumi, and Y. Shiohara, Physica C: Superconductivity and its Applications **357-360,** 1059-1062 (2001).